Magneto-Structural Correlations in Pseudotetrahedral Forms of the [Co(SPh)$_4$]$^{2-}$ Complex Probed by Magnetometry, MCD Spectroscopy, Advanced EPR Techniques, and ab Initio Electronic Structure Calculations

Elizaveta A. Suturina,[†,‡] Joscha Nehrkorn,[§] Joseph M. Zadrozny,[∥,⊥] Junjie Liu,[#,&] Mihail Atanasov,[†,∇] Thomas Weyhermüller,[†] Dimitrios Maganas,[†] Stephen Hill,[*,#,△] Alexander Schnegg,[*,§] Eckhard Bill,[*,†] Jeffrey R. Long,[*,∥] and Frank Neese[*,†]

[†]Max Planck Institute for Chemical Energy Conversion, Stiftstraße 34-36, Mülheim an der Ruhr 45470, Germany

[‡]Novosibirsk State University, Pirogova 2, 630090 Novosibirsk, Russia

[§]Berlin Joint EPR Lab, Institute for Nanospectroscopy, Helmholtz-Zentrum Berlin für Materialien und Energie, Kekuléstraße 5, 12489 Berlin, Germany

[∥]Department of Chemistry, University of California Berkeley, Berkeley, California 94720, United States

[⊥]Department of Chemistry, Northwestern University, Evanston, Illinois 60208, United States

[#]National High Magnetic Field Laboratory, Tallahassee, Florida 32310, United States

[&]Department of Physics, Clarendon Laboratory, University of Oxford, Parks Road, Oxford OX1 3PU, United Kingdom

[∇]Bulgarian Academy of Sciences, Institute of General and Inorganic Chemistry, Akad. Georgi Bontchev Street 11, 1113 Sofia, Bulgaria

[△]Department of Physics, Florida State University, Tallahassee, Florida 32306, United States

Ⓢ Supporting Information

ABSTRACT: The magnetic properties of pseudotetrahedral Co(II) complexes spawned intense interest after (PPh$_4$)$_2$[Co(SPh)$_4$] was shown to be the first mononuclear transition-metal complex displaying slow relaxation of the magnetization in the absence of a direct current magnetic field. However, there are differing reports on its fundamental magnetic spin Hamiltonian (SH) parameters, which arise from inherent experimental challenges in detecting large zero-field splittings. There are also remarkable changes in the SH parameters of [Co(SPh)$_4$]$^{2-}$ upon structural variations, depending on the counterion and crystallization conditions. In this work, four complementary experimental techniques are utilized to unambiguously determine the SH parameters for two different salts of [Co(SPh)$_4$]$^{2-}$: (PPh$_4$)$_2$[Co(SPh)$_4$] (**1**) and (NEt$_4$)$_2$[Co(SPh)$_4$] (**2**). The characterization methods employed include multifield SQUID magnetometry, high-field/high-frequency electron paramagnetic resonance (HF-EPR), variable-field variable-temperature magnetic circular dichroism (VTVH-MCD), and frequency domain Fourier transform THz-EPR (FD-FT THz-EPR). Notably, the paramagnetic Co(II) complex [Co(SPh)$_4$]$^{2-}$ shows strong axial magnetic anisotropy in **1**, with $D = -55(1)$ cm^{-1} and $E/D = 0.00(3)$, but rhombic anisotropy is seen for **2**, with $D = +11(1)$ cm^{-1} and $E/D = 0.18(3)$. Multireference ab initio CASSCF/NEVPT2 calculations enable interpretation of the remarkable variation of D and its dependence on the electronic structure and geometry.

1. INTRODUCTION

In the field of modern inorganic chemistry magneto-structural correlations in transition-metal complexes have been used (1) to rationally design molecules with desirable magnetic properties, for example, to maximize the anisotropy of the magnetic moment for single-molecule magnets,[1,2] and (2) to relate the magnetic properties to the electronic and geometric structures governed by the open d shell of the transition metal. In turn, such studies provide powerful tools to extract structural information about the active sites of metalloproteins.[3] In this context the tetrathiophenolate high-spin Co(II) complex (PPh$_4$)$_2$[Co(SPh)$_4$] (**1**) was synthesized first[4,5] to mimic isostructural [Fe^{II}(S-cysteine)$_4$]$^{2-}$ sites in the iron−sulfur protein rubredoxin, which binds Fe(II) by four cysteine ligands. The Co(II) ion in **1** represents a valuable EPR probe.[6] Due to

its half-integer spin of $S = 3/2$ and the high sensitivity of its magnetic and optical properties with respect to the coordination number and local symmetry, Co(II) has also been used to probe the coordination environment of integer-spin Fe(II) and spectroscopically silent Zn(II) sites of enzymes and proteins directly by substitution with the EPR-active ion.[7−9] Magneto-structural correlations of Co(II) ions have been employed for interpretation of the data, as established from well-characterized synthetic compounds. In the past the correlations have been rationalized by means of the angular overlap model (AOM),[10,11] whereas ab initio quantum chemical methods are the state of the art.[12−14]

High-spin Co(II) complexes are also interesting candidates for single-molecule magnet studies[15] because, due to strong spin−orbit coupling expected in pseudotetrahedral symmetry, even mononuclear complexes can possess large magnetic anisotropy and show slow relaxation of the magnetization.[16−27] Such slow relaxation hinges mostly on the easy-axis anisotropy of the magnetic moment enhanced by the large zero-field splitting (ZFS) of the electronic ground state. Slow relaxation of the magnetization has also been observed in four-coordinated Co(II) complexes with easy-plane and even nonaxial magnetic anisotropy but only with applied static magnetic field.[28,29] In attempts to enlarge the ZFS of pseudotetrahedral Co(II) compounds, softer ligand environments have been introduced for a series of four-coordinate complexes with heavy coordinating atoms, in particular sulfur.[19−22] The design of deliberately elongated tetrahedral environments to ensure that magnetic anisotropy is of the easy-axis type has also proven a successful strategy in this respect.[22−25] Recently, we employed multireference ab initio methods to explore how the anisotropy in π interactions of thiolate modulates the magnetism of such pseudotetrahedral Co(II) complexes by modification of the second coordination sphere.[12,13]

Once a pronounced easy-axis anisotropy is achieved, a plethora of experimental issues impede the accurate determination of ZFS and other SH parameters.[30] Conventional EPR frequencies, such as X-band (10 GHz, $h\nu = 0.33$ cm^{-1}) and Q-band (34 GHz, $h\nu = 1.13$ cm^{-1}), often yield no spectra because of the large magnitude of the ZFS (ranging from 10 to 100 cm^{-1}). The difficulties in the determination of ZFS by low-frequency EPR, stemming from the fact that the microwave quanta are orders of magnitude smaller than the energy splitting of the ground state,[31] can be partially circumvented by operating at high field (up to 35 T) and/or high frequency (up to the THz range, so-called HF-EPR).[32] In addition, field-sweep measurements at multiple frequencies, which yield a variety of resonance fields, can make profitable use of the competition of zero-field and Zeeman interactions for probing the systems. Recently, several inorganic compounds with a large ZFS,[32−35] including tetrahedral Co(II) complexes,[36−39] have been studied by field-sweep HF-EPR. However, the ZFS of spin manifolds can also be directly observed by microwave spectroscopy without or with constant external magnetic fields. Due to recent experimental improvements, frequency domain Fourier transform EPR (FD-FT THz-EPR) spectroscopy can now be employed in the determination of ZFS for such inorganic compounds.[40−45] Indeed, we use this technique here for an unambiguous and accurate direct measurement of the ZFS in the range from 10 to 125 cm^{-1}.

The experimental challenges in applying EPR spectroscopy to systems with large ZFS values often necessitate alternative

characterization techniques, such as SQUID magnetometry and magnetic circular dichroism (MCD) spectroscopy. The latter occupies a unique role within the family of electronic spectroscopies, because it provides information on the electronic and magnetic properties of the orbital ground state (e.g., spin states and SH parameters) as well as the excited orbital states. Hence, the method represents a link between ground state techniques, such as EPR/magnetometry, and excited states techniques, such as UV/vis/NIR electronic absorption spectroscopy. MCD spectra, recording the difference in the absorption of left and right circular polarized light, measure magnetically induced chirality, caused by longitudinal fields applied along the light path. MCD intensity arises from three different mechanisms, of which essentially only the so-called C-term contributions[46−49] are interesting for Co(II) compounds, since they are dominant, and arise from the unequal Boltzmann populations of the ground state magnetic sublevels. Therefore, SH parameters can be deduced from field- and temperature-dependent MCD intensity data (even without knowing the nature of the underlying optical transitions).[50−55] In addition to this information, which is complementary to SQUID magnetization data, the MCD intensities reveal so-called effective transition dipole moment products identifying the optical transitions. MCD bands have transition probabilities quite different from absorption bands and can be positive or negative, which sometimes helps to resolve overlapping absorption bands.

A multireference theoretical approach for ab initio calculations of spin Hamiltonian (SH) parameters is well established and widely used.[2,56] It is based on an effective Hamiltonian formalism that maps the SOC-CASSCF/NEVPT2 computed energy and wave function of the ground multiplet onto the phenomenological SH.[57] In contrast, the simulation and interpretation of MCD spectra with quantum chemical calculations are by no means straightforward. Only recently multireference approaches such as SOC-CASSCF/NEVPT2 have been used to estimate directly the difference in transition probabilities for left and right circularly polarized light in the presence of an external magnetic field using exact diagonalization rather than perturbation theory, and this approach has been proven to be quite successful.[58,59]

In this work, we analyze experimentally and theoretically the magnetic and spectroscopic properties of the $[Co(SPh)_4]^{2-}$ dianion in two different molecular salts, $(Ph_4P)_2[Co(SPh)_4]$ (**1**) and $(NEt_4)_2[Co(SPh)_4]$ (**2**). These compounds exhibit dramatically different magnetic properties, in spite of the fact that the paramagnetic centers are chemically identical. We demonstrate the power and limits of conventional and HF-EPR spectroscopy, MCD, SQUID magnetometry, and FD-FT THz-EPR for accurate evaluation of the SH parameters. A detailed analysis of the electronic structures, including the excited orbital states, on the basis of the absorption/MCD spectra and ab initio calculations gives a qualitative and quantitative picture for the magneto-structural correlations in the $[Co(SPh)_4]^{2-}$ complexes.

2. METHODS

2.1. Synthesis. All reactions were carried out in strictly anaerobic conditions under a nitrogen atmosphere using standard Schlenk techniques. Further details regarding the synthesis and the crystallographic data of compounds **1** and **2** are provided in the Supporting Information.

2.2. Spin Hamiltonian Simulations and Fitting. The magnetic properties of **1** and **2** have been analyzed by using the usual SH operator for mononuclear spin $S = 3/2$ that includes ZFS and Zeeman terms:

$$\hat{H}_S = D\left[\hat{S}_z^2 - \frac{1}{3}S(S+1) + \frac{E}{D}(\hat{S}_x^2 - \hat{S}_y^2)\right] + \mu_B \vec{B} \cdot \mathbf{g} \cdot \hat{\vec{S}} \quad (1)$$

where **g** is the electronic **g** matrix with diagonal elements g_x, g_y, and g_z and D and E/D are the axial and rhombic ZFS parameters. There are different conventions of identifying D and E parameters from a **D** tensor with canonical components D_{ii}. In this work we use the relations $D = D_{zz} - 1/2(D_{xx} + D_{yy})$ and $E = 1/2(D_{xx} - D_{yy})$. The rhombicity parameter E/D is limited to the range $0-0.33$ without violating generality by choosing the coordinate system such that $|D_{zz}| \geq |D_{yy}| \geq |D_{xx}|$. Note that collinearity of the **D** tensor and the **g** matrix is assumed here.[60]

The D- and E/D-dependent terms cause splitting (ZFS) of the quartet ground state into two Kramers doublets separated by an energy gap, which is given by eq 2.

$$2D' = 2\sqrt{D^2 + 3E^2} \quad (2)$$

In the limit of axial symmetry (i.e., when $E/D = 0$), the doublets are characterized by the spin projection quantum numbers $M_S = \pm1/2$ and $M_S = \pm3/2$, of which the latter is the ground state for $D < 0$ and vice versa. Finite rhombicity ($E/D > 0$) mixes wave function components differing by $\Delta M_S = \pm2$ but cannot lift the Kramers degeneracy. Magnetic fields applied in the z direction split the Kramers doublets according to their M_S values (Figure 1, top), whereas transversal fields in the x/y directions cause strong Zeeman splitting of the second

Kramers doublet but only weak splitting of the ground doublet (Figure 1, bottom) caused by mixing of M_S components differing by $\Delta M_S = \pm1$. Such pronounced easy-axis magnetic anisotropy of the ground Kramers doublet is essential for the reported single-molecule-magnet behavior of **1**.[17]

2.3. Weak Field Approximation. In the limit of weak magnetic fields, when Zeeman splitting is much smaller than ZFS, the Kramers doublets can be described using two effective spin $\tilde{S} = 1/2$ with corresponding effective **g** matrices, **g**′. The principal components of the two **g**′ matrices depend on D, E, **g**, and the magnetic field. Expanding the energies up to third order in $g_i\mu_B B/D'$, one obtains[31]

$$g'_i = g_i\left\{1 \pm \frac{2(\alpha_i D + 3\gamma_i E)}{D'} \mp \left(\frac{g_i\mu_B B}{D'}\right)^2\left(\frac{\alpha_i D + 3\gamma_i E}{D'}\right)\right.$$
$$\left. \times \left[1 - \left(\frac{\alpha_i D + 3\gamma_i E}{D'}\right)^2\right]\right\} \quad (3)$$

where $i = x, y, z$, $\alpha_x = \alpha_y = 1/2$, $\alpha_z = 1$, $\gamma_x = \gamma_y = 1/2$, $\gamma_z = 0$, and the upper (lower signs) relate to the Kramers doublets with $\tilde{M}_S = \pm3/2$ and $\tilde{M}_S = \pm1/2$, respectively (the tilde emphasizes that due to nonzero E and transversal field other M_S values can be admixed within the wave function). For axial symmetry with $E = 0$, $g_z = g_\parallel$, and $g_x = g_y = g_\perp$, the effective values for the Kramers doublets, are given by eqs 4 and 5, respectively.

$$g'_z\left(\tilde{M}_S = \frac{3}{2}\right) = 3g_z \quad g'_\perp\left(\tilde{M}_S = \frac{3}{2}\right) = 2g_\perp\left[\frac{3}{16}\left(\frac{g_\perp\mu_B B}{D}\right)^2\right] \quad (4)$$

$$g'_z\left(\tilde{M}_S = \frac{1}{2}\right) = -g_z \quad g'_\perp\left(\tilde{M}_S = \frac{1}{2}\right) = 2g_\perp\left[1 - \frac{3}{16}\left(\frac{g_\perp\mu_B B}{D}\right)^2\right] \quad (5)$$

2.4. Magnetic Measurements. Magnetic susceptibility data were measured in the temperature range $2-270$ K by using a SQUID susceptometer with an applied field of 0.1 T (MPMS-7, Quantum Design, calibrated with a standard palladium reference sample, error <2%). Sample holders made of quartz and equipped with O-ring seals were used, and the polycrystalline powder samples of solid material were immobilized using minute amounts of eicosane (melting point 310 K) to prevent torqueing of crystallites in large magnetic fields. Multiple-field variable-temperature magnetization measurements were performed at 1, 4, and 7 T in the range $2-260$ K with the magnetization sampled at regular intervals on an inverse ($1/T$) temperature scale. The SQUID response curves (raw data) were corrected for holder and eicosane contributions by subtracting the corresponding response curves obtained from separate measurements without a sample. The desired magnetization data were obtained from the amplitudes of the corrected SQUID response curves by appropriate curve fitting. The sample magnetization values were divided by the number of moles and converted to molar susceptibility units according to the definition $\chi = \mu_0 M/B$, and these experimental χ values were subsequently corrected for underlying diamagnetism by use of tabulated Pascal's constants, as well as for temperature-independent paramagnetism (TIP). Handling and simulation of the SQUID raw data as well as spin-Hamiltonian simulations of the derived susceptibility and magnetization data were performed after the measurements using the software package julX for exchange-coupled systems (available from E.B.). Magnetic moments were derived from the eigenfunctions of the spin Hamiltonian (eq 1) by using the Hellman−Feynman theorem:

$$\vec{\mu}_i(\vec{B}) = -\langle\Psi_i|d\hat{H}/d\vec{B}|\Psi_i\rangle \quad (6)$$

The powder summations were obtained by using a 16-point Lebedev grid.

2.5. X- and Q-band EPR Spectroscopy. X-band continuous wave (cw) EPR measurements were performed on a Bruker E500 ELEXSYS
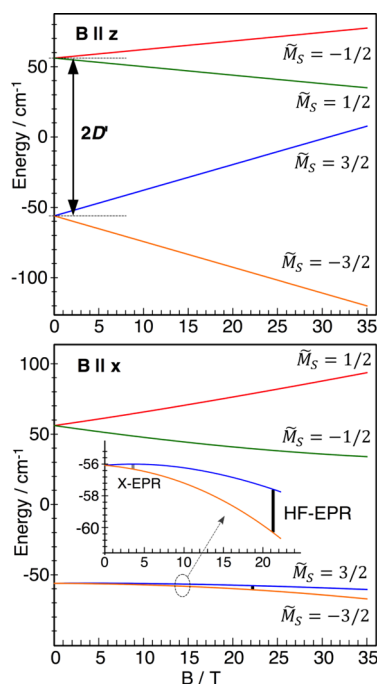

Figure 1. Example of energy levels of a spin quartet with quasi-axial zero-field splitting ($D = -55$ cm^{-1}, $E/D = 0.03$) calculated from eq 1 as a function of strong magnetic fields applied along molecular z (top) and x (bottom) directions with $\mathbf{g} = (2.03, 2.03, 2.61)$. The situation applies for the HF-EPR measurements of complex **1** treated below. The black vertical bars in the bottom panel indicate the weakly allowed HF-EPR transition within the low-lying Kramers doublet for fields applied in the xy plane, as observed in single-crystal measurements. The labeling of the spin levels by effective $\tilde{M}_S$ values follows the convention introduced below for weak field approximations. Due to this formalism the relative order of $-1/2$ and $+1/2$ levels in the upper panel are inverted, in accordance with eq 3.

c

spectrometer equipped with a Bruker dual-mode cavity (ER4116DM) or a standard cavity (ER4102ST) and an Oxford Instruments helium flow cryostat (ESR 900). The microwave unit was a high-sensitivity Bruker Super-X (ER-049X) bridge with integrated microwave frequency counter. The magnetic field controller (ER032T) was externally calibrated with a Bruker NMR field probe (ER035M). Q-band cw-EPR measurements were performed on a Bruker ESP-300E spectrometer with a Bruker Q-band cavity (ER5106QT) with Bruker flexline support and an Oxford Instruments helium cryostat (CF935). Microwave frequencies were measured with a Hewlett-Packard frequency counter (HP5352B), and the field control was calibrated with a Bruker NMR field probe (ER035M). Spectra were recorded at 10 K with 0.5 mW microwave power and 0.75 mT/100 kHz modulation at X-band and with 50 μW microwave power 2 mT/100 kHz modulation at Q-band. Resolved spectra were simulated with the software package esim_gfit (available from E.B.), which employs the effective spin approximation by using two effective spins $S' = 1/2$ for the two Kramers doublets of the quartet and two separate effective **g** tensors, $\mathbf{g}'(3/2)$ and $\mathbf{g}'(1/2)$, for parametrization (eqs 4 and 5).

2.6. High-Field EPR Spectroscopy. HF-EPR data were collected with a spectrometer that enabled in situ rotation of a single-crystal sample about a fixed axis, as described in detail elsewhere.[61,62] Signals were located by incremental rotation of the crystal followed by successive spectral measurements until the field was aligned along an axis within the molecular plane of hard magnetization. A discernible signal was only obtained over an impressively small 2.5° arc of crystal orientations out of the hard plane. A 36 T resistive magnet at the National High Magnetic Field Laboratory of Florida State University generated the fields for the measurements. A Millimeter vector network analyzer and several different multipliers were used as the microwave source (50−106 GHz) and the detector.

2.7. Frequency Domain Fourier Transformed EPR (FD-FT THz-EPR) Spectroscopy. FD-FT THz-EPR experiments were conducted at the THz beamline of the BESSY II storage ring. The FD-FT THz-EPR setup is described elsewhere in detail.[42,63] Samples of ~40 mg of polycrystalline **1** and **2** were pulverized together with 100 mg of high-density polyethylene (PE) in a glovebox under an argon atmosphere and pressed into pellets of 1/2 in. (~12.7 mm) diameter with a thickness of ~2 mm. THz coherent synchrotron radiation (THz-CSR) extracted from BESSY II operated in low-α storage-ring mode and a Hg-arc lamp were used as the radiation sources in the spectral ranges 10−40 and 30−200 cm^{-1}, respectively.[64] FD-FT THz-EPR requires reference measurements to discriminate EPR transitions from standing waves in the beam path and nonmagnetic absorption in the samples. Therefore, raw data spectra were divided by a reference spectrum taken on the same sample but at different temperature or field. Simulations of the FD-FT THz-EPR spectra were performed employing a recently developed approach implemented in *EasySpin*.[65,66]

2.8. Magnetic Circular Dichroism (MCD) and Absorption Spectroscopy. MCD experiments were carried out with finely dispersed powders embedded in KBr pellets on an Olis DSM17 CD spectropolarimeter, equipped with an Oxford Instruments Spectromag SM4000 cryostat for temperature and field control of the sample compartment. The temperature was varied in the range from 2 to 80 K, and spectra were recorded in the energy range from 5000 to 30000 cm^{-1} (2000 to 333 nm). In addition, electronic absorption spectra were recorded on the same samples with the Olis DSM17 instrument at 20−80 K, as well as with a Cary spectrometer (Model 6000i, Agilent Technologies) equipped with an Oxford Instruments Optistat-DN cryostat set to 80 K. Global fits with Gaussian lines were performed for consistent temperature and field series of MCD as well as absorption spectra with an in-house program (mcd_bf). Line positions were kept identical throughout the series, but line widths were allowed to vary as a function of temperature by 10−20%.

At the peak positions of the MCD spectra we carried out variable-temperature variable-field (VTVH) MCD experiments in which the MCD intensity was measured at a fixed wavelength, at multiple temperatures and varying magnetic fields, in order to probe C-term behavior. The results are presented as isotherms of the MCD intensity

vs $\mu_B B/2kT$, where μ_B is the Bohr magneton, k is Boltzmann's constant, B is the strength of the applied field, and T is the absolute temperature. The VTVH magnetization curves, which showed a pronounced nesting behavior as expected for MCD C-term signals from $S > 1/2$ systems, were simulated using our program mcd3D_S2 (available from E.B.) for global fits, which is based on the equation

$$\frac{\Delta\varepsilon}{E} = \frac{\gamma}{4\pi S} \int_0^\pi \int_0^{2\pi} \sum_i N_i (l_x \langle \hat{S}_x \rangle_i M_{yz}^{\text{eff}} + l_y \langle \hat{S}_y \rangle_i M_{zx}^{\text{eff}} + l_z \langle \hat{S}_z \rangle_i M_{xy}^{\text{eff}}) \sin\theta \; d\theta \; d\phi \qquad (7)$$

developed by Neese and Solomon for MCD C-term signals from systems with nondegenerate orbital ground states.[50] Here, $\Delta\varepsilon/E$ is the MCD intensity, γ is a collection of constants, S is the total spin of the ground state, N_i is the Boltzmann population of the ith magnetic sublevel of the electronic ground state, $l_{x,y,z}$ are the directional cosines of the angles between the magnetic field and the molecular coordinate system of the spin Hamiltonian, and $\langle S_{x,y,z} \rangle_i$ are the expectation values of the x, y, z components of the spin operator $\hat{S}$ over the ith magnetic eigenstate, respectively. The spin expectation values were obtained from the same spin Hamiltonian used for the simulation of magnetic susceptibility and EPR data (eq 1), and identical spin Hamiltonian parameters were employed for all VTVH curves of a sample. The factors M_{vw}^{eff} ($v, w = x, y, z$) are effective transition dipole moments, independently determined for every transition, from which individual polarizations of the MCD bands can then be calculated by using the relation

$$\% \; x = 100 \frac{(M_{xy}^{\text{eff}} \cdot M_{xz}^{\text{eff}})^2}{(M_{xy}^{\text{eff}} \cdot M_{xz}^{\text{eff}})^2 + (M_{xy}^{\text{eff}} \cdot M_{yz}^{\text{eff}})^2 + (M_{xz}^{\text{eff}} \cdot M_{yz}^{\text{eff}})^2} \qquad (8)$$

for the percentage of x polarization and its permutations to obtain the corresponding y and z components of the polarization.[50]

2.9. Computational Details. All calculations were carried out using the ORCA 3.0[67] quantum chemistry computational package. Geometry optimization and frequency calculations were performed with the BP86 functional,[68,69] Ahlrichs polarized basis set def2-TZVP,[70−72] and Grimme's dispersion correction D3.[73,74] The resolution of identity approximation was employed with auxiliary basis set def2-TZVP/J in order to speed up the calculations.[75]

Absorption and MCD spectra,[76] as well as SH parameters, were computed using state-averaged complete active space self-consistent field (SA-CASSCF).[77,78] The missing dynamic correlations were recovered by N-electron valence perturbation theory to the second order (NEVPT2).[79,80] The segmented all-electron relativistically contracted version[81] of Ahlrichs polarized basis set def2-TZVP[70−72] and the second-order Douglas−Kroll−Hess[82] (DKH) were employed to account for the scalar relativistic effects. The active space was chosen to contain seven electrons in five cobalt 3d-based molecular orbitals. All states arising from the d^7 configuration (10 quartets and 40 doublets) were taken into account. The spin−orbit coupling (SOC) was treated using the mean field (SOMF) approximation[83] as implemented in ORCA. The effective Hamiltonian approach[84,85] was used to compute SH parameters.

3. RESULTS

3.1. Structure. The crystal structures of compounds **1** and **2** (Table S1 in the Supporting Information) show that different counterions engender different local geometries around the Co(II) center in the two salts of $[\text{Co}(\text{SPh})_4]^{2-}$ (Figure 2). In both cases the average Co−S bond length is ~2.32 Å, but the S−Co−S angles vary significantly. In the case of **1**, four S−Co−S angles are larger than the tetrahedral angle (109.47°) and two are smaller, while in the case of **2**, it is the other way around (Table S2 in the Supporting Information). Hence, the structure of the CoS$_4$ core corresponds to an elongated tetrahedron for **1** and compressed tetrahedron for **2**. Therefore, one can
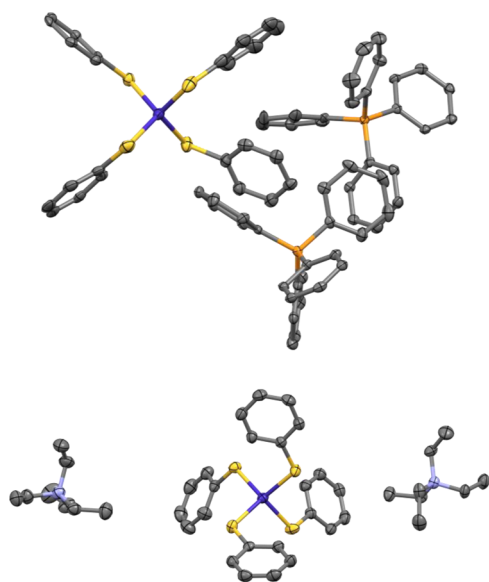
Figure 2. X-ray crystallographic structures of (top) $(PPh_4)_2[Co-(SPh)_4]$ (**1**) and (bottom) $(NEt_4)_2[Co(SPh)_4]$ (**2**). Dark blue, yellow, orange, light blue, and gray ellipsoids represent cobalt, sulfur, phosphorus, nitrogen, and carbon atoms, respectively.

approximately define the S_4 rotational axis for $[Co^{II}(SPh)_4]^{2-}$ as pointing out of the plane of Figure 2.

The four S−Co−S−C torsion angles for **1** and **2** are close to 180 and $\pm 50°$, indicating that the coordination environments are good approximations of D_{2d} and S_4 symmetries, respectively.

3.2. Magnetic Susceptibility Data. Temperature- and field-dependent magnetic susceptibility measurements were performed in an effort to determine ZFS and g parameters of the Co(II) complexes in **1** and **2** in the solid state (Figures 3A and 4A). Above 150 K, polycrystalline samples showed almost constant values of $\chi T = 2.48$ and 1.97 cm³ K/mol for **1** and **2**, respectively. These are both larger than the spin-only value for $S = 3/2$ (1.875 cm³ K/mol), revealing significant orbital contributions to the magnetic moments, in particular for **1**. The values are specifically sensitive to the g factors of the spin quartet ground states of both compounds, because, in a spin Hamiltonian description, the high-temperature limit of χT is proportional to $g^2 S(S + 1)$. However, accurate measurements depend critically upon the purity of the samples and correct assessment of the diamagnetic and TIP contributions to χ,[12] as will be discussed below.

The χT curves for both compounds decline at low temperatures, beginning at 120 and 40 K for **1** and **2**, respectively, indicating thermal depopulation of the excited Kramers doublet as a result of a large ZFS. As the onset temperatures of the decay for **1** and **2** are measures of ZFS, the data suggest strikingly different ZFS parameters for **1** and **2**, although their paramagnetic $[Co(SPh)_4]^{2-}$ anions are chemically identical. Iso-field magnetization curves were measured at 1, 4, and 7 T for accurate determinations of the axial and rhombic ZFS parameters D and E/D. Here, data were sampled at equally spaced intervals on a $1/T$ scale (Figures 3B and 4B). This detection mode emphasizes the low-temperature range, and the field effects probe zero-field interactions independent from Boltzmann depopulation of levels through the increasing Zeeman perturbation of the spin system. Note that the magnetization data for **1** and **2**, as presented in Brillouin
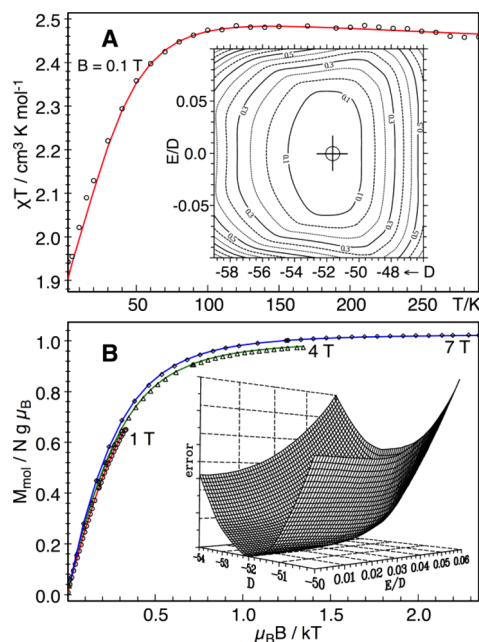
Figure 3. (A) Temperature dependence of χT for **1** obtained with a polycrystalline sample immobilized in an eicosane matrix and measured with a field of $B = 0.1$ T. (B) Iso-field magnetization data recorded at 1, 4, and 7 T. The solid lines are the result of a global spin Hamiltonian simulation with $D = -51.5$ cm^{-1} and $E/D = 0.002$, $g_{x,y} = 2.084$, $g_z = 2.591$. The insets show different views of the relative fit errors as a function of D and E/D, with the best fit marked with a cross in (A). The experimental data are corrected for diamagnetism, $\chi_{dia} = -587 \times 10^{-6}$ cm³/mol, and TIP-like contributions, $\chi_{TIP} = +814 \times 10^{-6}$ cm³/mol.
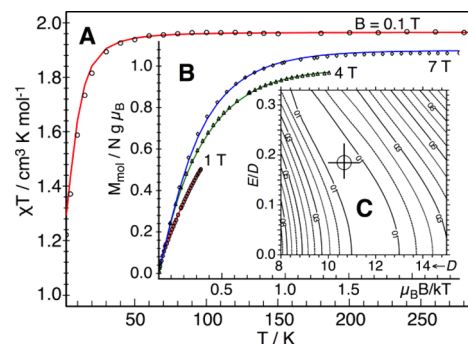

Figure 4. Temperature dependence of χT for **2** obtained with a polycrystalline sample in a field of $B = 0.1$ T. (B) Iso-field magnetization data recorded at 1, 4, and 7 T. The solid lines are the result of a global spin Hamiltonian simulation with $D = +10.6$ cm^{-1} and $E/D = 0.18$, $g_{x,y} = 2.112$, $g_z = 2.076$. The inset shows relative global fit errors as a function of D and E/D, with the best fit marked with a cross. The experimental data have been corrected for diamagnetism, $\chi_{dia} = -387 \times 10^{-6}$ cm³/mol, and TIP-like contributions, $\chi_{TIP} = +350 \times 10^{-6}$ cm³/mol.

coordinates $\mu_B B/kT$, level off below 1.5 μ_B, the expected value for isotropic spin $S = 3/2$. Thus, these data suggest a quite strong orbital contribution to the magnetic moment. The spread, or nesting, of the saturation magnetization curves for **2** is the result of a contention between ZFS and Zeeman effects, whereas the curves for **1** lack such nesting behavior. In this case the field independence does not indicate an absence of ZFS but rather a very strong magnetic anisotropy that renders the ground levels to behave as a quasi-isolated Kramers doublet.

Similar behavior has been observed for strongly anisotropic non-Kramers systems.[86] Apparently, the applied fields of 1, 4, and 7 T can hardly affect the nature of the ground state Kramers doublet for **1**, but they do in the case of **2**. The unusual behavior of **1** is explained by energetic isolation of this doublet, which on the one hand impedes the magnetic field from affecting the Boltzmann distribution and on the other hand hampers field-induced mixing of the doublets. It further suggests a vanishing E/D parameter, which otherwise would mix the doublets. This qualitative interpretation of the magnetic data for **1** summarizes the previous analyses invoked to explain its reported SMM behavior.[17]

Consistent SH simulations of the SQUID data for **1** and **2** with global fitting of χT and magnetization curves, as shown in Figures 3 and 4, corroborate the foregoing explanation. Best fit values are found at $D = -52(2)$ cm^{-1} and $E/D = 0.00(3)$ with $g_{x,y} = 2.08(9)$, $g_z = 2.6(2)$, $\chi_{TIP} = +[814(80)] \times 10^{-6}$ cm^3/mol for **1** and $D = +11(2)$ cm^{-1} and $E/D = 0.18(4)$ with $g_{x,y} = 2.1(1)$, $g_z = 2.1(3)$, $\chi_{TIP} = +[350(70)] \times 10^{-6}$ cm^3/mol for **2**. The error ranges were obtained from inspection of the error contour plots shown in the insets of the figures, as well as from single-point calculations along the contour lines. Interestingly, the sign of the large D value is unambiguously negative for **1** but positive for **2**. Global fits for **2** with negative D values iterated quickly to a robust alternative global minimum, although it turned out to be an improper representation (with $E/D > 0.33$) of the values given above.

The relative large uncertainty of the g_z values reflects the large uncertainty in TIP-like contributions, which could not be defined without fitting. The large TIP value of $814(80) \times 10^{-6}$ cm^3/mol found in this procedure for **1** is close to typical values tabulated for quasi-tetrahedral Co(II) complexes ($(505-789) \times 10^{-6}$ cm^3/mol).[87] The lower TIP correction found for **2** ($[350(70)] \times 10^{-6}$ cm^3/mol) compares well with TIP of Co(II) complexes with nondegenerate ground states (350×10^{-6} cm^3/mol).[88] If we adopt genuine TIP, originating from field-dependent state-mixing under LS coupling,[88] the different values support an assumption of the first excited electronic state of **2** being higher in energy than for **1**.

The large g anisotropy found for **1** with $g_{x,y} = 2.08(9)$ and $g_z = 2.6(2)$ is significant and reflects the negative slope of the $\chi T(T)$ data of **1** above 200 K: increasing thermal populations of the $\tilde{M}_S = \pm \frac{1}{2}$ Kramers doublet (which has an easy xy plane of magnetization in contrast to the easy z axis of the ground state $\tilde{M}_S = \pm 3/2$ doublet) turn the major contribution to the powder magnetization from the g_z direction at low temperatures to the $g_{x,y}$ plane at high temperature (see Figure 1 for the corresponding Zeeman splitting). In contrast, the temperature dependence of χT for **2** does not indicate significant g anisotropy and the fits could have been restrained to an isotropic average g factor.

3.3. X- and Q-band EPR Spectra. Conventional cw-EPR spectroscopy can provide detailed insight into the magnetic properties of half-integer spin systems **1** and **2**, which is complementary to the macroscopic information obtained from the SQUID measurements. We specifically applied this technique to achieve constraint on the rhombicity parameters of both compounds better than that permitted by magnetometry. Spectra were collected at liquid helium temperatures with polycrystalline powder samples, which avoids ambiguous solvation effects. The spectra suffer from enhanced line broadening by intermolecular dipole interactions. In agreement with previous EPR experiments,[89] the powder X-band EPR
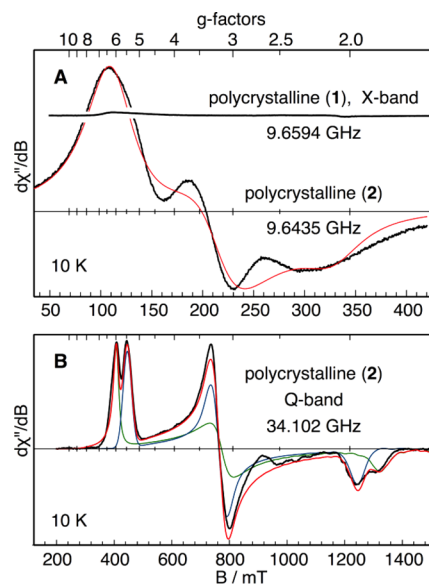

Figure 5. (A) X-band EPR spectra of polycrystalline powders of **1** and **2** recorded at 10 K. (B) Q-band EPR spectrum of polycrystalline **2** recorded at 10 K. Experimental conditions: (A) 0.5 mW power, 0.75 mT modulation; (B) 50 μW power, 2 mT modulation. The red line in (A) is a simulation with effective g values given in the text, and in (B) it is a spin Hamiltonian simulation with two subspectra shown in green ($E/D = 0.21$, **g** = (2.3, 2.3, 2.1)) and blue ($E/D = 0.18$, **g** = (2.2, 2.2, 2.15)). D was fixed and set to 10.6 cm^{-1} for both subspectra.

spectrum of **1** was essentially found to be silent (Figure 5A, top trace). A very weak signal without hyperfine splitting appeared around $g' = 6.3$ but has to be assigned to traces of a paramagnetic impurity (see also an estimate of the forbidden transition in Figure S7 in the Supporting Information). A similar impurity with $g' = 5.68$ was observed previously by Fukui et al.[11] for the Zn/Co 1% doped powder samples of the tetramethylammonium salt $(Me_4N)_2[Co(SPh)_4]$. In contrast, a weak signal at $g' = 7.8$ with fully resolved ^{59}Co hyperfine splitting, as was previously reported for a 10% Co/Zn doped powder preparation and which has been assigned to the g_z' transition of the $\tilde{M}_S = \pm 3/2$ Kramers doublet,[6,89] was not observed in our experiments, neither with a pure solid sample nor with a 10% doped Co(II)/Zn(II) polycrystalline powder of **1**.

EPR silence of the spin quartet compound **1** is expected for powder samples at X-band frequency because of the large anisotropy of the ground state $\tilde{M}_S = \pm 3/2$ doublet arising from the large negative D value and axial symmetry, $E/D \approx 0$ (Figure 1). The corresponding powder spectra would be exceedingly broad with vanishing small transition probability for the low-field $\Delta M = 3$ transition at g_z'. The g_{xy}' transitions are partially allowed due to M_S mixing by the transversal field, but they would occur at high fields of ~4 T, beyond the range of usual X- and Q-band spectrometers (see Figure 5). In fact, the absence of a detectable g_z' signal from the powder samples provides an upper limit for the rhombicity of **1**, for which we obtained $0 \leq E/D \leq 0.03$ by comparison of the derivative amplitudes of a series of simulated spectra with the signal to noise ratio of the measurements. This result does not narrow down the range of the E/D values as derived from the SQUID analysis, necessitating the application of the techniques given later in the paper.

It is a general problem that ZFS values this large prevent direct detection of excited states, and temperature-dependent population/depopulation experiments (which enable accurate determination of the sign of D) are prevented due to the onset of fast spin relaxation at temperatures slightly above liquid helium temperature. Line broadening due to dipolar interactions in the solid state is another prohibitive issue for such compounds.[6,11,89] Attempts to alleviate line broadening by dilution in frozen solution require careful analyses, because results can be obscured by unknown structural variations upon solvation. Further efforts to suppress dipole broadening by doping the Co(II) target complexes into diamagnetic zinc hosts can also lead to uncontrolled structural modifications that drastically affect the magnetic properties of the Co(II) ions.[6,11]

Polycrystalline samples of **2** showed distinct X-band EPR spectra, as depicted in Figure 5A. The lines are broadened, as expected for a solid-state sample (FWHM values of Lorentz lines are (35, 39, 43) mT), but approximate effective g' values (6.2, 3.2, 2.1) could be obtained from a fit. Accounting for the poor accuracy, this is in reasonable agreement with previously reported data for a magnetically diluted sample in a 1% Co/Zn doped polycrystalline solid: $g' = (5.4, 3.05, 1.9)$.[6] Interestingly, at Q-band frequency, the nondilute sample of **2** showed fully resolved derivative lines and distinct g splitting (Figure 5B), but still without resolved HFS. The higher resonance fields in comparison to X-band apparently afforded increased g splitting on the field axis without line broadening (in field units). This behavior indicates enhanced decoupling of the intermolecular spin−spin interactions. However, to our surprise, the outer lines of the powder spectrum both showed a small splitting, which may be explained by the presence of two slightly different species in the sample (despite the fact that XRD analysis predicts only one unique magnetic center in a unit cell). Since this was not observed by X-ray diffraction for **2**, it is possible that a thermally induced separation of sites occurred below the temperature of the crystal structure determination (100 K).

The two subspectra of the rhombic complex **2** have effective g' values ((5.5, 3.1, 1.98) and (6.0, 3.2, 1.86)) that both can be assigned to two similar $\tilde{M}_S = \pm 1/2$ Kramers doublets with large rhombicity parameters. The Lorentz line broadening with (28, 100, 80) and (40, 60, 70) mT FWHM for the first and second components, respectively, was used in the simulation (Figure 5B). A simulation yielded $(E/D)_1 \approx 0.18$ and $(E/D)_2 \approx 0.21$ (blue and green lines in Figure 5B). Both E/D values are consistent with the SQUID result, 0.18(4). Attempts to corroborate the ZFS values by X- or Q-band EPR by measurements at elevated temperatures with populated excited levels failed, because the spectra broadened beyond recognition. The electronic g values obtained from the EPR simulations, $g_1 = (2.3, 2.3, 2.1)$ and $g_2 = (2.2, 2.2, 2.15)$, are slightly higher than the (average) values $g_{x,y} = 2.1(1)$ and $g_z = 2.1(3)$ from magnetic measurements for **2**, which may be explained by a minor (3%) diamagnetic contamination of the SQUID sample.

3.4. High-Field Electron Paramagnetic Resonance Spectra. High-field electron paramagnetic resonance (HF-EPR) measurements were performed with a single crystal of **1** (dimensions <1 × 1 × 1 mm³) to search for EPR resonances that are inaccessible at standard magnetic field strengths. Careful angle-dependence studies were first performed at a relatively low frequency of 49.92 GHz by incrementally rotating the crystal about a fixed axis until the applied magnetic field was within 1° of the hard plane of magnetization, where a single

EPR absorption was discovered around 25 T (Figure 6). It is notable that the observed transition quickly broadens and
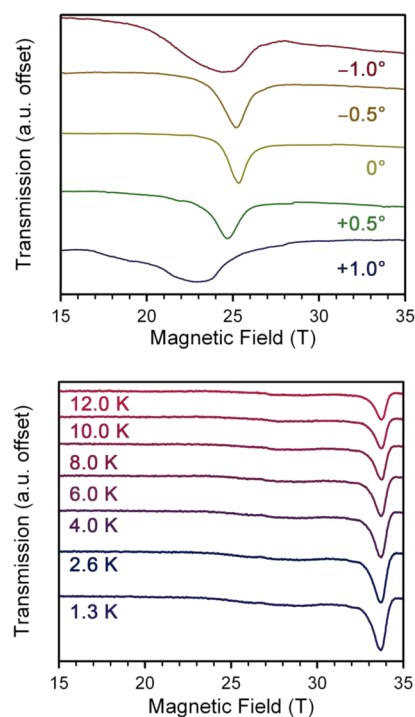

Figure 6. (top) Single-crystal HF-EPR resonances of **1** as a function of the angle between the molecular hard plane of magnetization and the applied magnetic field. The measurements were performed at 1.3 K and 49.92 GHz; transmission signals are shown, where the dips correspond to resonances. (bottom) Temperature dependence of the HF-EPR transmission spectra at 104.16 GHz, with the magnetic field oriented in the hard plane of the molecules. The intensity of the resonance at 33 T increases with decreasing temperature, indicating that it is a ground state transition.

disappears when the direction of the magnetic field rotates only a few degrees out of the hard plane. Such behavior confirms the proposed strong axial type magnetic anisotropy of the $\tilde{M}_S = \pm 3/2$ Kramers doublet of **1**. The intensity of the transition increases with decreasing temperature, indicating a ground state origin for the observed resonance.

The variable-frequency EPR spectra and the frequency vs resonant field dependence of the observed high-field transition are presented in Figure 7. These data were collected at the field orientation where the EPR transition appears at the highest magnetic field, which necessarily corresponds to the field alignment closest to the molecular hard plane (due to the experimental limitation of crystal rotation about a single axis, the azimuthal angle ϕ of the field orientation within the hard plane was not known). At 49.92 GHz, a resonance is detected at 25 T, which rapidly moves to higher field with increasing microwave frequency, ultimately moving past the 35 T window of the magnet above 104.16 GHz. The frequency dependence of the transition was simulated using the SH (eq 1) under the assumptions that $B_z = 0$ and $g_x = g_y = g_\perp$

$$\hat{H}_S = D\left[\hat{S}_z^2 - \frac{1}{3}S(S+1) + \frac{E}{D}(\hat{S}_x^2 - \hat{S}_y^2)\right]$$
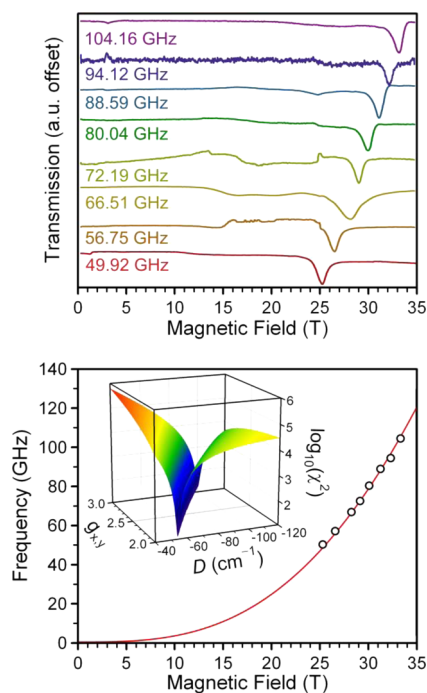$$+ \mu_B g_\perp B(\hat{S}_x \cos\varphi + \hat{S}_y \sin\varphi) \tag{9}$$

Figure 7. (top) Variable-frequency single-crystal HF-EPR transmission spectra for $(Ph_4P)_2[Co(SPh)_4]$ (**1**) with the magnetic field applied in the hard plane of the molecule. Data were collected at 1.3 K. The features seen between ~15 and 25 T in some traces are due to a mechanical instability of the setup at high fields and were ignored in the data analysis. (bottom) Frequency dependence of the resonance fields at 1.3 K. The red line is a simulation of the frequency dependence of the resonance field for an $S = 3/2$ species with $g_\perp = 2.08$ and $D = -57$ cm^{-1}. Inset: 3D contour plot of the error $(\log_{10} \chi^2)$ associated with fitting the frequency dependence of the resonant fields as a function of $g_\perp$ and D. Values of $\log_{10} \chi^2$ range from 5.8 (red) to 1 (dark purple).

The rhombic anisotropy term, $E(\hat{S}_x^2 - \hat{S}_y^2)$, was first set to 0, due in part to the experimental limitation of only one crystal rotation axis, but also because the electronic structure, the magnetization data, and X-band EPR measurements all suggest it should be small. As shown in Figure 7, excellent agreement is obtained between experiment and simulation, which strongly suggests that the observed resonance corresponds to the transition within the $\tilde{M}_S = \pm 3/2$ ground Kramers doublet, which splits in a strong magnetic field applied in the hard plane, as shown in Figure 1. Similar to conventional low-field EPR, the large ZFS in **1** precluded the observation of the $\tilde{M}_S = \pm 3/2$ to $\tilde{M}_S = \pm 1/2$ inter-Kramers and $\tilde{M}_S = \pm 1/2$ intra-Kramers doublet transitions. Since the frequency-dependent HF-EPR measurements reported here were restricted to a single field orientation, they define only a single resonance as a function of field, which is equivalent to knowledge of only one effective g' value in eq 4. Consequently, the resonance field is proportional to $D/\sqrt{g_\perp^3}$, and equal quality fits are therefore obtained over a range of $g_\perp$ (from 2 to 3) and D values (-54 to -120 cm^{-1}), as shown in the inset to Figure 7. Nevertheless, the data clearly indicate a very large, negative zero-field splitting in **1**. Moreover, if one constrains the HF-EPR fit using the value of $g_\perp = 2.08$ determined from the magnetization measurements, a D value of $-57(1)$ cm^{-1} (ZFS, $2D = 114(2)$ cm^{-1}) is obtained, which is quite consistent with the other measurements presented in this study, as discussed below. This is a very reasonable thing to do because the $g_\perp$ value is well constrained

from the fits to the magnetization data for **1**, as previously discussed. Thus, one already sees here the benefits of a multimethod approach to the measurement of SH parameters in highly anisotropic transition-metal complexes, as has been noted also in several other recent combined magnetic and HF-EPR investigations.[34,35]

Finally, we consider the influence of a nonzero $E(\hat{S}_x^2 - \hat{S}_y^2)$ term on the determination of D and $g_\perp$ through the HF-EPR data. Due to the fact that we were only able to perform single-axis rotation, the field orientation in the molecular hard plane, φ, remains an arbitrary experimental parameter. A small E term can slightly influence the hard-plane frequency dependence, leading to corrections to the correlation between $g_\perp$ and D in our model. The influence of a nonzero E term is shown in Figure S1 in the Supporting Information. The analysis is performed by allowing E to vary between 0 and 3 cm^{-1}, while allowing φ to vary in the fit. The results demonstrate that a small value $(E < D/20)$ does not affect the analysis very significantly. The main effect is to slightly broaden the minimum in the $\log_{10} \chi^2$ error surface, while the correlation between $g_\perp$ and D remains essentially the same. The net effect, therefore, is a slightly larger uncertainty in the best fit D value $(\Delta D = 2.6$ cm$^{-1})$ corresponding to a given value of $g_\perp$.

3.5. FD-FT THz-EPR Spectra. Direct measurements of the very large ZFS in **1** and **2** required very high excitation frequencies. Thus, we applied FD-FT THz-EPR spectroscopy by which high-energy EPR transitions between the $\tilde{M}_S = \pm 3/2$ and $\tilde{M}_S = \pm 1/2$ Kramers doublets with energy gap $2D'$ can be probed in the range between 10 and 200 cm^{-1}. Measurements on a polycrystalline powder sample of **1** with intense THz-CSR yielded several transitions in the energy range between 20 and 37 cm^{-1}, but none of them showed any changes upon applying an external magnetic field. Due to the very high sensitivity of the FD-FT THz-EPR setup to EPR transitions in the spectral range between 10 and 37 cm^{-1}, we concluded that **1** has no EPR transitions in this range for fields below 1 T.

A broader energy range from 30 to 200 cm^{-1} was probed with an Hg-arc lamp as the radiation source. Figure 8A depicts experimental and simulated FD-FT THz-EPR magnetic-field division spectra (MDS). MDS were obtained by dividing raw spectra taken at different external magnetic fields as indicated on the y axis. This method strongly suppresses nonmagnetic peaks and allows for an assignment of EPR peaks by their field dependence. In Figure 8B is depicted a simulation obtained from the division of the calculated EPR absorption lines at 3 T (Figure 8C) and 1 T (Figure 8D) at $T = 5$ K. Line widths in the simulations were adjusted to match the experimental spectra. The observed broad lines are assumed to result from powder averaging of all possible molecular orientations with respect to B_0 as well as strains in the D and g values.

The resulting calculated line is plotted in the bottom spectrum of Figure 8A alongside the measured FD-FT THz-EPR MDS. This spectrum is characterized by two minima around 115 and 107 cm^{-1} and a center maximum at 110 cm^{-1} (see Figure 8A bottom traces, MDS 3 T/1 T). The maximum and the second minimum were identified as significant (deviation from one exceeds two standard deviations; see the Supporting Information). With increasing magnetic field, the negative MDS parts at 115 and 107 cm^{-1} shift to higher and lower energies, respectively. Finally, in the MDS obtained at (8 T)/(6 T) and (9 T)/(7 T) the magnetic field induced absorption changes are hardly visible. This may be rationalized by an increase of the overall EPR line width due to the
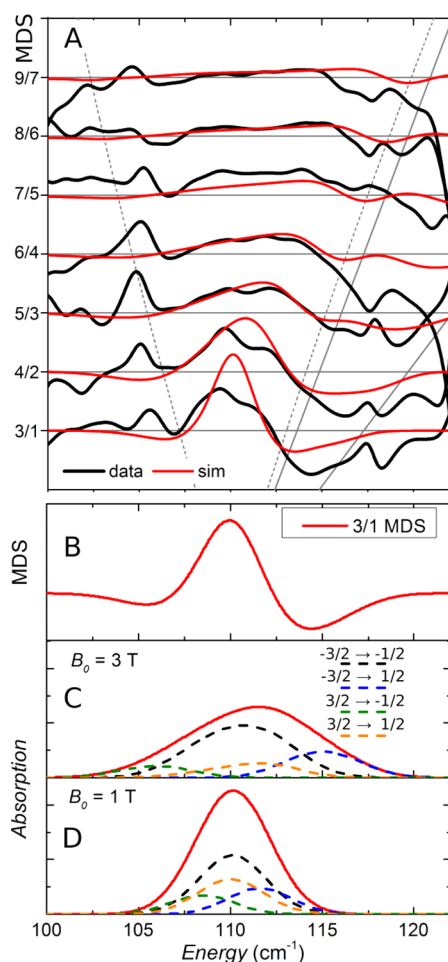
Figure 8. (A) Experimental (black) and simulated (red) FD-FT THz-EPR spectra of **1** measured at $T = 5$ K and the indicated fields between 1 and 9 T in the range 100−125 cm^{-1}: magnetic field division spectra (MDS) of **1** (black solid lines) derived in each case from two absorption spectra recorded at the fields indicated on the left side. Corresponding SH simulations are shown in red (for details see text). The thin gray lines indicate the transition energies of the transition between the Kramers doublets for $B_0 \| z$ (solid) and $B_0 \perp z$ (dashed). (B) Demonstration of the construction of the calculated MDS obtained by division of two simulated absorption spectra for $B_0 = 3$ and 1 T. (C, D) Calculated powder EPR absorption spectra for $B_0 = 3$ and 1 T, respectively. The absorption of the individual $\tilde{M}_S \rightarrow \tilde{M}_S'$ transitions are shown as dashed lines (for the definition of $\tilde{M}_S$ see Figure 1). All simulations were done with the following SH parameters: $D = -55$ cm^{-1}, $E/D = 0$, $\mathbf{g} = (2.1, 2.1, 2.6)$.

increasing Zeeman splitting and the fact that parts of the EPR spectrum are probably shifted in a spectral region where they overlap with strong nonmagnetic absorptions, in either the sample (80−100 cm^{-1}) or the z-cut quartz windows separating the compartments of the sample magnet (125−135 cm^{-1}). The field dependence of the MDS bands clearly indicates magnetic transitions, the observation of which, at almost 4 THz (133 cm^{-1}), is rare and demonstrates the unique abilities of the employed FD-FT THz-EPR setup. The SH simulations of the MDS pattern (Figure 8A, red traces) revealed high sensitivity to the total ZFS, $2D'$, of the spin quartet of **1** but virtual insensitivity to the rhombicity parameter E/D and the sign of D. Therefore, E/D was fixed to 0. In addition, changes in the g values had only a slight effect on the simulated spectra. Due to this fact, we used g values obtained from fits to the

magnetization: $g_x = g_y = 2.1$ and $g_z = 2.6$ (vide infra). In summary, the FD-FT THz-EPR measurements cannot contribute to the determination of the rhombicity and g value of **1** but can provide a unique and accurate value for the total ZFS: namely, $2D' = 110(2)$ cm^{-1}. This value is not obscured by sample purity issues or unknowns such as TIP for the SQUID measurements or by the severe covariance problems of g and D values encountered upon the SH simulations for the HF-EPR measurements. With the reasonable approximation $0 \leq E/D \leq 0.03$, we obtain $|D| = 55(1)$ cm^{-1} with very high confidence. The maximun uncertainty for the rhombicity, $E/D = 0.03$, causes only a minor deviation for the axial parameter, according to eq 2.

FD-FT THz-EPR measurements of **2** using THz-CSR in the energy range from 10 to 37 cm^{-1} revealed several transitions (Figure S3 in the Supporting Information). However, only one transition at 24.9 cm^{-1} showed magnetic-field dependence. It exhibits significant broadening at fields up to 0.5 T and, at 1 T, a resolved splitting. Therefore, this absorption was assigned to an EPR transition, which represents at zero magnetic field a direct observation of the ZFS of the ground quartet state.

In accordance with the case of **1**, the SH simulations for **2** were again sensitive to ZFS, whereas the rhombicity parameter E/D and the g anisotropy influenced the simulations only for fields of 0.5 T and above. However, the simulations could reproduce only a part of the experimental data for any reasonable value of E/D and g factors. Hence, these parameters are poorly defined from this experiment and, at best, the isotropic part of g could be estimated. However, the value $g_{iso} = 2.7(3)$, is unreliably large and not consistent with the X- and Q-band EPR spectra shown above. The total ZFS, which is derived from the common center of the field-dependent transition, is more reliable and yields $2D' = 25(1)$ cm^{-1} for **2**, in agreement with the corresponding SQUID magnetometry results, i.e., $D = +11(2)$ cm^{-1} and $E/D = 0.18(4)$, which, according to eq 2, yield $2D' = 24(4)$ cm^{-1}.

3.6. Variable-Temperature Variable-Field (VTVH) Magnetic Circular Dichroism. Magnetic circular dichroism (MCD) and electronic absorption spectra were recorded for **1** and **2** to explore further the electronic ground and excited states and to relate them with structural properties. Here, we present MCD intensity data recorded at variable temperatures in the range from 2 to 80 K, with variable fields ranging from 0 to 10 T (VTVH MCD data), and their analysis in terms of SH parameters for probing the magnetic ground states of **1** and **2**. At first glance, the vis/NIR MCD as well as the absorption spectra of both compounds look rather similar to distinctly structured bands around 6000 and 14000 cm^{-1} for **1**, of which mainly the low-energy regime is ∼1000 cm^{-1} upshifted for **2** (Figure 9). The intensities of the MCD bands depend strongly not only on the applied field but also on temperature (Figure 9), which reveals a C-term mechanism for all of them. The strong C terms arise from differences in the Boltzmann populations of the ground state magnetic sublevels and correspondingly varies with field and temperature.[50] For instance, MCD intensities recorded at 10 T and 5 K decrease by nearly a factor of 2 when the temperature is increased from 5 to 40 K (Figure 9A,B). In detail, however, as the temperature further decreases (or the field increases), the MCD intensities are no longer linear with respect to $\mu B/kT$, as implied by eq 6; they instead level off to their saturation limits (Figure 9C,D).

Such VTVH-MCD data were recorded at 10 band energies. The curves recorded at 6135 cm^{-1} for **1** and 6386 cm^{-1} for **2**
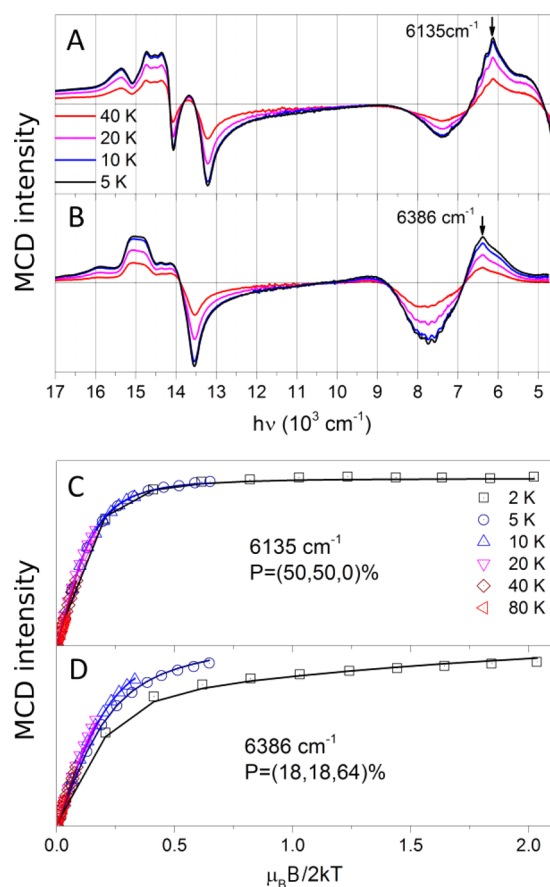
Figure 9. Variable-temperature MCD spectra of **1** (A) and **2** (B) at 10 T and VTVH MCD isotherm data for the selected bands at 6135 (C) and 6386 cm^{-1} (D), respectively, together with best fit lines obtained from spin Hamiltonian simulations according to eq 6 and with parameters given in the text.

are shown in Figure 9C,D. Similar to the SQUID magnetization data (Figure 3), the VTVH MCD saturation curves are spread for **2** but not for **1**, due to the much larger zero-field splitting in **1** than in **2**. Simultaneous fitting of all VTVH curves for each compound was performed with a unique set of SH parameters, but with independent polarization factors for the different electronic transitions (eq 6). The resulting SH parameters are consistent with the observations from the other methods but did not substantially improve the precision of the SH parameters (for details see a remark in the Supporting Information). Analyses of the fit error surfaces (Figure S4 in the Supporting Information) show that, for **1**, D falls in the interval from −20 to −90 cm^{-1} and g_z is in the interval from 2.6 to 2.9, while $g_{x,y}$ was fixed at 2.1; the data appeared not to be sensitive to E/D. In the case of **2**, the VTVH MCD spectra show that $|D|$ is in the interval from 3 to 13 cm^{-1} and g is in the interval from 1.8 to 3.

3.7. MCD and Absorption Spectra. Powder absorption and MCD spectra of **1** and **2** in the visible and near-IR regions contain two bands: one from ~5000 to 10000 cm^{-1} and another from ~12000 to 19000 cm^{-1}. In order to analyze the transitions forming the spectra, we performed a simultaneous deconvolution of absorption and MCD spectra using Gaussian functions. A minimum of 14 and 13 Gaussians for compounds **1** and **2**, respectively, are required to successfully fit the absorption and MCD spectra simultaneously. Details regarding the chosen Gaussian functions for both **1** and **2** are presented

in Tables S4 and S5 in the Supporting Information, respectively. It should be highlighted that, although such a deconvolution is not unique and can also be achieved with a different number of Gaussian functions and/or different sets of line widths and intensities, in a first approximation it provides a qualitative description of the spectra.

As can be seen in Figure 10, the two compounds exhibit rather similar spectra, with a few important differences. Close
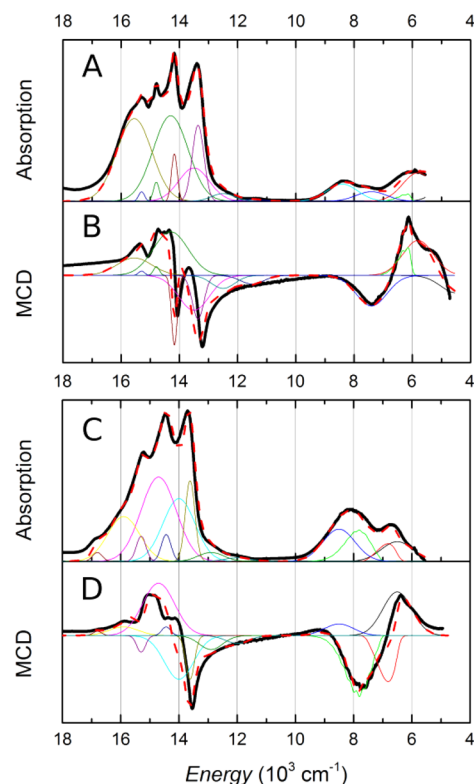

Figure 10. Deconvolution of absorption spectra of mull samples of **1** (A) and **2** (C) recorded at 80 K and MCD of mull samples of **1** (B) and **2** (D) recorded at 2 K and 10 T. Colored lines are individual transitions, and red dashed lines are the sums of all individual contributions. Bands around 7000−8000 cm^{-1} are simulated with vibrational progression with characteristic frequency ~200 cm^{-1}.

inspection of the absorption that occurs between 4000 and 10000 cm^{-1}, in particular at the edge of the MCD spectra located at 4500−5000 cm^{-1}, reveals a difference in sign of the MCD signals for **1** and **2**. There is no MCD intensity for the absorption band located at 8400 cm^{-1} in the spectra of **1**, while for **2**, the maximum in absorption at ~8000 cm^{-1} corresponds to a strong negative signal in the MCD spectrum. The higher energy section of the spectra, from 10000 to 18000 cm^{-1}, also contains notable differences. The first sharp absorption band is found at higher energy for **2** in comparison to **1**: 13600 versus 13100 cm^{-1}, respectively. Furthermore, the shape and energy distribution of the four sharp absorption features in this energy range vary substantially for the two compounds. In the case of **1**, there are two sharp MCD negative features located at 13100 and 14100 cm^{-1} while, in the case of **2**, only one negative spectral feature is observed at 13500 cm^{-1}. The variation in the energies and MCD behavior of these transitions reveals significant information about the differing electronic structures of **1** and **2**. As will be seen in the next section, a quantitative
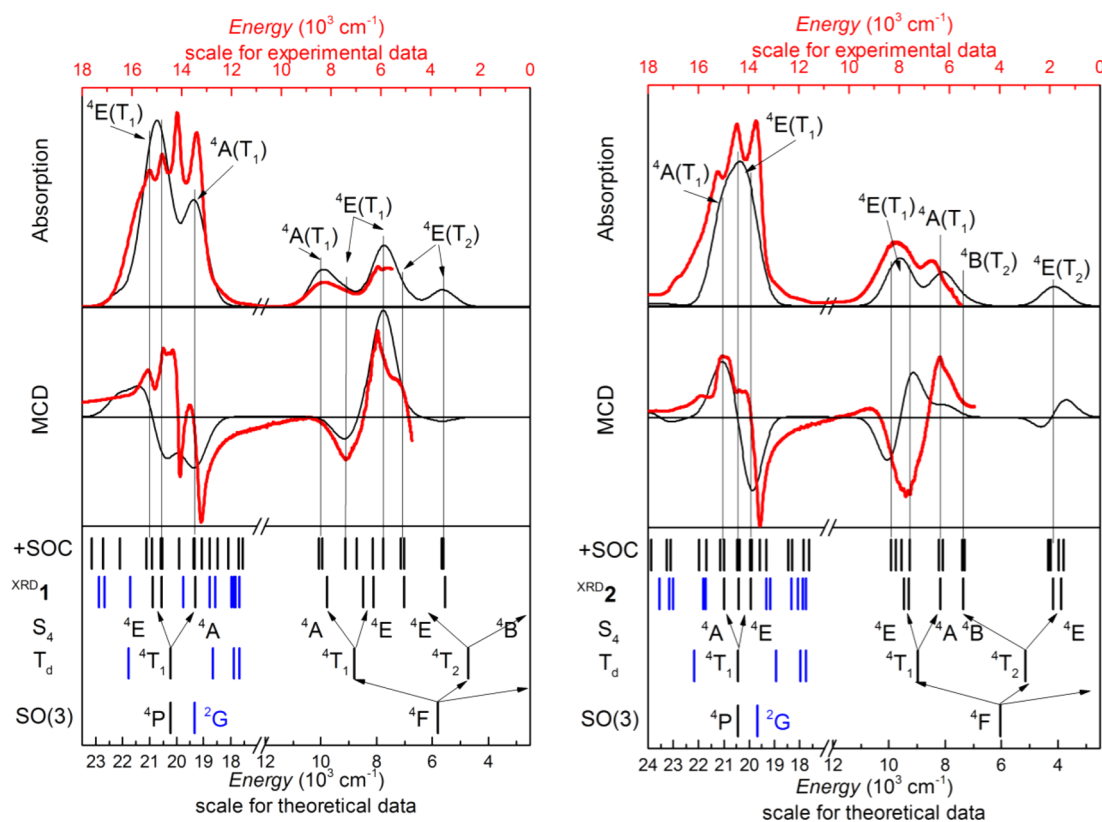
Figure 11. Comparison of the experimental (red) and theoretical (black) absorption and MCD spectra for **1** (left) and **2** (right). Theoretical spectra were obtained by SOC-CASSCF(7,5)/NEVPT2 calculations with Gaussian line broadening (FWHM 1000 cm^{-1}). Underlying electronic states for theoretical spectra are shown in the bottom panels: +SOC corresponds to the SOC corrected energies, and ^{XRD}**1** and ^{XRD}**2** energies correspond to nonrelativistic states computed for X-ray structures of **1** and **2**. Assignment of the main bands is done in terms of the S_4 symmetry group (an approximate symmetry of the molecule); vertical lines for main bands are shown for guidance. Parent terms for idealized tetrahedral symmetry (T_d) and corresponding free ion terms (SO(3)) are shown. The energy scale for the theoretical result (bottom axis) is offset to compensate for the overestimated interelectronic repulsion and permit better comparison to experiment (see text for details).

description of the observed bands with the aid of quantum chemical calculations enables key chemical insights.

3.8. Computational Results. *3.8.1. Excited States and Spectra.* In an effort to arrive at qualitative and quantitative descriptions of the experimental bands, we computed the respective absorption and MCD spectra for the crystallographic structures of $[Co(SPh)_4]^{2-}$ in **1** and **2** on the basis of the relativistic SOC-CASSCF(7,5)/NEVPT2 functional. The observed differences in spectra between **1** and **2** at low energies (4000−10000 cm^{-1}) are reproduced extremely well by the calculations (Figure 11). The difference in the splitting of the MCD bands of **1** and **2** at higher energies (12000−18000 cm^{-1}) is also well reproduced. However, the energy of this band is overestimated by the theory (see the energy scales for the experimental and theoretical spectra in Figure 11). The reason for this discrepancy is an overestimated interelectronic repulsion that originates from the lack of dynamic correlation in the CASSCF method. This lack is partially corrected by NEVPT2, but not enough to lead to energy agreement.

The energies of the spin−orbit coupled states used for spectral simulation are marked "+SOC" in the lowest panel of Figure 11. It is clear that many states contribute to each band and assignment of the bands in terms of these relativistic states would be quite tedious. Thus, the assignment is done in terms of the nonrelativistic states (marked as ^{XRD}**1** and ^{XRD}**2** in Figure 11), where quartet states are depicted in black and doublet states in blue. Both quartet and doublet states are overlaid in

the high-energy band. This overlap explains the appearance of the sharp features observed in the low-temperature spectra. The natural line width for the "spin-forbidden" transition to doublet states is much smaller than that for allowed transitions to quartet states. Thus, at low temperature, when thermal broadening is small, the nature of the transition is manifested in the total line width.

The labeling of the nonrelativistic states is done in terms of the S_4 symmetry group, because both structures are quite close to this symmetry. However, there is a small but perceptible splitting of the E states caused by distortions away from ideal symmetry in the crystal structures of **1** and **2** (see the underlying states marked ^{XRD}**1** and ^{XRD}**2** in Figure 11). The parent terms of the idealized tetrahedral structure (T_d) and corresponding free ion terms (SO(3)) are shown below at the mean energies of the corresponding nonrelativistic states. Parameters of the ligand field theory can be directly extracted from this diagram. For example the ligand field strength, $10Dq$, is the energy of the $^4T_2$ term ($\sim$5000 cm^{-1}), whereas the Racah parameter B of the interelectronic repulsion is computed as the difference between the ^4F and ^4P spectroscopic terms divided by 15 ($B \approx 970$ cm^{-1}). The value of B is slightly larger than that in experiment, owing to overestimated energy of the high energy band originating from the ^4P term. Since the difference in energy of the ^2G and ^4F atomic band positions is $4B + 3C$, the C/B value is estimated to be $\sim$3.3. All of these results are in agreement with our previous studies.[12]

As shown in Figure 11, the geometrical differences of complexes **1** and **2** engender a reversal of the tetragonal splitting in each triplet state T. For example, the first excited term $^4T_2$ for **1** splits into ^4B (lower energy) and ^4E (higher energy) while, for **2**, the ordering of the states is reversed. In fact, this state interchange is responsible for the different signs of D (for a detailed discussion, see ref 12), and it also affects the spectra. Further, the three low-energy bands are split at almost equal energy intervals (6000, 8000, and 10000 cm^{-1}) for **1**, whereas for **2** the first band is shifted to lower energy (4000, 8000, and 10000 cm^{-1}), as shown in the theoretical spectra in Figure 11. In both cases, there is a distinct line at ∼10000 cm^{-1}. However, the origin of the transitions is different, which becomes obvious in the theoretical MCD spectra: for **1** there is no MCD signal, but in the case of **2** there is a derivative-shaped transition in the MCD spectrum. The derivative-shaped MCD signal corresponds to a ^4E state; it appears because of the splitting of the components of ^4E due to spin−orbit coupling as well as symmetry lowering. One can see that the splitting of $^4E(^4T_1)$ is mostly due to spin−orbit coupling, whereas $^4E(^4T_2)$ splits because of symmetry lowering. The transition to the ^4A state in **1** has a large intensity in absorption but no intensity in MCD, because it is purely z polarized. However, in **2**, it gains a small amount of intensity by mixing with E states. The difference in the shape of the band at 18000−22000 cm^{-1} is also associated with the reversed order of ^4E and ^4A states in **1** and **2**. The contribution of the doublet states here is also significant. Indeed, around $^4T_1(^4P)$ states there are at least 14 doublet states originating from the parent ^2G and ^2P atomic spectroscopic terms. However, state mixing makes an unambiguous assignment of the spin-forbidden transitions very difficult. Nevertheless, the comparative analysis of the theoretical and experimental spectra allowed us to assign most of the transitions obtained by the simultaneous deconvolution of the MCD and absorption spectra (Figure 10; the assignments are given in Tables S4 and S5 in the Supporting Information), revealing the connection between the geometry and the spectral properties of **1** and **2**.

3.8.2. Structures. Analysis of the D3-BP86/def2-TZVP geometry optimization data of the $[Co(SPh)_4]^{2-}$ complexes **1** and **2** provides several local minima which are close to the corresponding experimental structures and differ by only a few kilocalories per mole (Table S3 in the Supporting Information). More specifically, at geometries around the crystallographic structure of complex **1** (denoted as ^{XRD}**1**), two idealized isomeric structures can be identified with local S_4 and C_2 symmetries, respectively (denoted as ^{S4}**1** and ^{C2}**1**). On the other hand, at geometries around the crystallographic structure of complex **2** (denoted as ^{XRD}**2**), only one isomer is identified, which possesses a compressed CoS_4 core, denoted as ^{S4}**2** in Table 1. Importantly, the SH parameters display great sensitivity to the local coordination environment in this family of complexes. Thus, in addition to the X-ray structures of **1** and **2**, the computationally idealized structures will be assessed for their SH parameters.

3.8.3. Spin Hamiltonian Parameters. As has been shown in previous studies,[13] calculations of the SH parameters of $[Co(SPh)_4]^{2-}$ require multireference methods with explicit treatment of the excited states and spin−orbit coupling that mixes those states. The SH parameters of $[Co(SPh)_4]^{2-}$ computed for the structures obtained from the X-ray diffraction (XRD) analysis reveal a significant dependence of the magnetic properties on the geometries of first and second coordination

Table 1. Spin Hamiltonian Parameters of Various Conformations of $[Co(SPh)_4]^{2-}$ Computed by SOC-CASSCF(7,5)/NEVPT2 Using the Effective Hamiltonian Approach

		D (cm^{-1})	E/D	g_x	g_y	g_z
^{XRD}**1**	CASSCF	−59.1	0.03	2.18	2.24	2.90
	NEVPT2	−46.7	0.03	2.14	2.18	2.71
^{S4}**1**	CASSCF	−64.0	0.00	2.16	2.16	2.91
	NEVPT2	−48.0	0.00	2.12	2.12	2.69
^{C2}**1**	CASSCF	−55.7	0.03	2.16	2.26	2.85
	NEVPT2	−42.2	0.04	2.12	2.17	2.65
^{XRD}**2**	CASSCF	16.6	0.16	2.41	2.47	2.22
	NEVPT2	11.5	0.16	2.29	2.33	2.16
^{S4}**2**	CASSCF	5.3	0.00	2.34	2.34	2.27
	NEVPT2	3.0	0.00	2.23	2.23	2.19

spheres. Like the experiments, the computed SH parameters reveal a large and negative D for **1** (with small rhombicity) and with easy-axis **g** matrix anisotropy. For **2**, the computed SH parameters indicate easy-plane anisotropy of the **g** matrix and a much smaller D value relative to **1** with considerable E/D. For these results, CASSCF calculations systematically give larger ZFS and principal g values in comparison to NEVPT2. Optimized structures with S_4 symmetry have pure easy plane or easy axis anisotropy, and therefore $g_x = g_y$ and $E/D = 0$ due to ideal degeneracy of the excited states of E symmetry. Thus, nonzero rhombicity implies the presence of distortions away from S_4 symmetry, which might appear due to crystal-packing forces. As discussed above, however, there is another C_2-symmetric conformer that corresponds to a local minimum in the gas phase which is slightly higher in energy than all of the others. The SH parameters of this conformer are closer to those derived by employing the crystallographic structure of complex **1**.

The computed effective **g**′ matrix of the lowest Kramers doublet also reflects the difference in the type of anisotropy of the conformers (Table 2). The lowest Kramers doublet of ^{XRD}**1**

Table 2. Effective g' Matrix of Lowest Kramers Doublets for Various Conformations of $[Co(SPh)_4]^{2-}$ Computed by SOC-CASSCF(7,5)/NEVPT2

	g'_x	g'_y	g'_z
^{XRD}**1**	0.19	0.20	8.10
^{S4}**1**	0.00	0.00	8.05
^{C2}**1**	0.27	0.28	7.91
^{XRD}**2**	3.43	5.65	2.01
^{S4}**2**	3.99	3.99	1.99

has a g'_z value of 8.1 (see eqs 4 and 5). The nonzero values of $g'_{x,y}$ in this case are due to nonzero rhombicity; in the case of the S_4 conformers, E/D is strictly 0 so that $g'_{x,y}(3/2) = 0$. For the ^{XRD}**2** conformer $g'_{x,y} > g'_z$. However, the difference between g'_x and g'_y shows that E/D is not 0, unlike the the case for the S_4 conformer.

3.8.4. Magneto-Structural Correlations. In an effort to further explore the sensitivity of the SH parameters with respect to structural conformations, we have constructed the two-dimensional CASSCF/NEVPT2 potential energy surface for a $[Co(SPh)_4]^{2-}$ model complex (Figure 12), where θ is the angle between the S_4 rotational axis and the sulfur atom of each SPh$^-$ ligand and ψ is the torsion angle between the plane containing
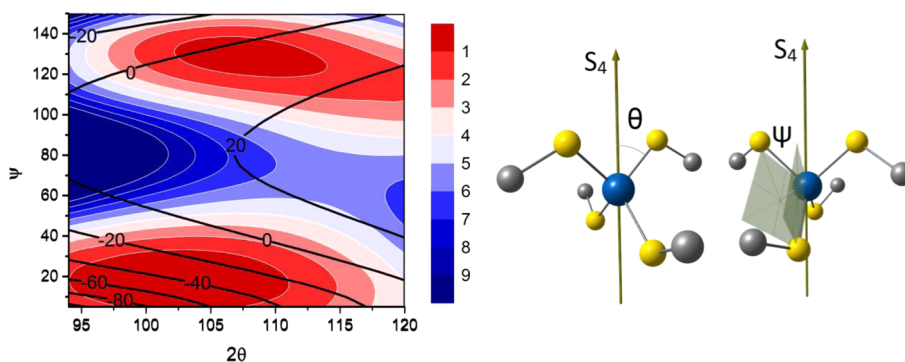
Figure 12. Potential energy surface (colors represent the relative energy in kcal/mol computed by BP86/def2-TZVP) together with ZFS isolines (black lines, values in cm^{-1}) computed by SOC-CASSCF(7,5) for optimized structures of $[Co(SCH_3)_4]^{2-}$. The definitions of the angles θ and ψ are shown on the right.

Table 3. Spin Hamiltonian Parameters Obtained with Different Experimental Methods

method	D (cm^{-1})	E/D	g_z	$g_{x,y}$
	Compound **1**			
powder susceptibility[16]	−62(1)	fixed at 0	2.960(3)	2.285(4)
powder magnetization at 2−5 K and 7 T[17]	−74[a]	<0.01[a]	2.91[a]	
powder susceptibility[6]	−100(30)	fixed at 0	3.13(?)	2.25(?)
single-crystal susceptibility[89]	−70(10)	fixed at 0	2.7(1)	2.2(1)
single-crystal EPR on Co/Zn 10%[89]		<0.09	2.6(1)	fixed at 2.2
powder susceptibility and magnetization at 0.1, 1, 3, and 7 T (this study)	−52(2)	0.00(3)	2.6(2)	2.08(9)
FD-FT THz-EPR (this study)	$(D^2 + 3E^2)^{1/2} = 55(1)$			
high-field EPR (this study)	−55	fixed at 0		fixed at 2.08
	Compound **2**			
powder susceptibility[6]	$(D^2 + 3E^2)^{1/2} = 5(1)$		2.27[a]	
powder EPR Co/Zn 1%[6]		0.19(2)	2.16[a]	
powder susceptibility and magnetization at 0.1, 1, 3, and 7 T (this study)	+11(2)	0.18(4)	2.1(1)	
FD-FT THz-EPR (this study)	$(D^2 + 3E^2)^{1/2} = 12.5(5)$			

[a]Errors were not reported in the study.

the S_4 axis and the sulfur atom and the plane formed by the bonded C−S−Co atoms; all other parameters were optimized. In an effort to restrict our analysis to the factors that influence the structural conformation within the first coordination sphere, while keeping the computational cost low, we focused the calculations on the model system $[Co(SCH_3)_4]^{2-}$. There are two minima on the potential energy surface. One corresponds to an elongated tetrahedron ($2\theta < 109.5°$) with a small torsion angle ψ, so that the symmetry is close to D_{2d}, whereas the second minimum is shifted toward a compressed tetrahedron with a large torsion angle. Both minima are quite shallow, with an energy barrier between the two structures of ~5 kcal/mol (according to CASSCF). This agrees well with the observations that, in solution, many conformations can be present, while in a crystal different conformations might be stabilized depending on the counterion.

Analysis reveals a strong dependence of D with respect to both ψ and θ. Specifically, D varies between −100 and +30 cm^{-1} within the thermally accessible conformations. For the conformers compressed along the S_4 axis D is positive while, for the respective elongated conformers, D is negative, depending mostly on the θ angle (Figure 12).

The ab initio analysis of the magneto-structural correlation shown above rationalizes the most preferable conformations found for the $[Co(SPh)_4]^{2-}$ dianion and the corresponding SH parameters, as a function of the most critical structural parameters θ and ψ.

4. DISCUSSION

Taken together, the results of X-ray diffraction and DFT gas-phase geometry optimization permit rationalization of the key factors that determine the geometrical structure of the $[Co(SPh)_4]^{2-}$ complexes in **1** and **2**. In both cases, the dianion adopts symmetries lower than tetrahedral. In fact, the tetragonal distortion caused by the ligand−ligand repulsion is reflected in both the crystallographic and DFT optimized structures. There is a clear correlation of the CoS$_4$ core tetragonal distortion and the orientation of the thiolate ligands: an elongated tetrahedron comes together with a small torsion angle ($\psi = 12°$), and a compressed tetrahedron comes with a large torsion angle ($\psi = 139°$). A similar bistability and correlation of θ and ψ angles, caused by interligand repulsion rather than a Jahn−Teller (or pseudo Jahn−Teller) effect, was found for tetrathiolato iron complexes and analyzed in great detail by means of AOM and DFT methods.[90] The deviation of the optimal ψ angle from 0° for the elongated structure is due to π anisotropy of the ligand which, for example for a π-isotropic phenolate-type ligand, yields the optimal torsion angle $\psi = 0°$.[12]

In addition, the combined analysis of the experimental and theoretical results indicates the structural dependence of the magnetic properties of **1** and **2**. In fact, complex **1** is EPR silent in the standard X-band EPR spectrum, due to the large effective **g** matrix anisotropy of the ground Kramers doublet (although Fukui and co-workers reported a weak signal with hyperfine

structure for a 10% doped Zn single crystal of **1** at low field, which gives a g_z value of 2.6 and $E/D < 0.09$.[6]

On the other hand, the X-band EPR spectrum of **2** is very broad, while the respective Q-band spectrum reveals the existence of two slightly different species in the sample. Simultaneous spin Hamiltonian simulations of the two subspectra results in $D = 10.6$ cm^{-1}, $E/D = 0.21$, **g** = (2.3, 2.3, 2.1) and $E/D = 0.18$, **g** = (2.2, 2.2, 2.15) for the two species (Figure 5, green and blue). These values agree well with the previously reported SH parameters extracted from 1% doped Zn powder spectra ($g = 2.16$ and $E/D = 0.19$).[6]

Unlike EPR spectroscopy, magnetometry does not indicate inhomogeneity in samples of **2**, and SH parameters from susceptibility data can be affected by diamagnetic and paramagnetic impurities. Another problem that can arise in magnetometry is partial alignment of the microcrystals (torquing) that affects the measured magnetic moment of the sample. These factors often generate discrepancies between SH parameters extracted from susceptibility measurements by different groups. To illustrate this point, Table 3 gives reported SH parameters for **1** from powder susceptibility measurements and from single-crystal susceptibility and EPR measurements. Thus, our experiments highlight the need for proper acknowledgment of the inherent uncertainty of SH parameters obtained from bulk susceptibility analyses. Thankfully, this uncertainty was resolved by our application of FD-FT THz-EPR, which revealed $|D| = 55(1)$ cm^{-1}, assuming a maximum value of $E/D < 0.03$, in accord with low-temperature magnetization experiments and conventional EPR spectra. As seen in Table 3, this value agrees very well with those extracted from our magnetometry and HF-EPR measurements. Unlike a previous study, the susceptibility fit in this work includes a TIP correction, as its exclusion would lead to overestimation of $|D|$.[12] We note that the ZFS parameters we obtain for **2** from magnetometry are likewise in agreement with FD-FT THz-EPR results (Table 3).

In a second step, we calculated the SH parameters for both complexes **1** and **2** by using the effective Hamiltonian approach via SOC-CASSCF/NEVPT2 calculations, which are in good agreement with the experimental consensus values (Table 1). Importantly, the electronic structure calculations here indicate that the key factor defining the ground state magnetic properties of the $[Co(SPh)_4]^{2-}$ complex is the spin–orbit coupling that mixes the ground state ($^4A_2$) with the excited states, where the largest contribution comes from the three lowest quartet states ($^4T_2$). Therefore, the splitting of these lowest-lying $^4T_2$ states defines the type and magnitude of the magnetic anisotropy. Likewise, our analyses of the absorption and MCD spectra shows that the degeneracy of both the $^4T_1(F)$ and $^4T_1(P)$ states is altered substantially by the changes in the coordination geometry of the cobalt ion in **1** and **2**. Here, the observed difference in the shift of the MCD signal relative to the absorption maxima (at 8500 cm^{-1} for **1** and 8000 cm^{-1} for **2**) suggests an interchanged order of the z and xy polarized components of $^4T_1(F)$ between the two compounds. This switch in order is likely the origin of the flip in sign of D between the two species.

5. CONCLUSIONS

Experimental determination of the spin Hamiltonian (SH) parameters in systems with strong zero-field splitting is a central challenge to developing magneto-structural correlations. In this work, the complexes $(PPh_4)_2[Co(SPh)_4]$ (**1**) and $(NEt_4)_2[Co$-

$(SPh)_4]$ (**2**), the former of which possesses extremely large zero-field splitting, were interrogated with an array of state of the art analytical techniques. Specifically, we employed SQUID magnetometry, EPR, HF-EPR, MCD, and FT-FD THz-EPR spectroscopy, as well as ab initio multiconfigurational computational analyses. Critically, we showed that previous interpretations based only on dc magnetometry resulted in incomplete and, in some cases, contradictory descriptions of the SH parameters. In fact, standalone magnetometry studies proved to be insensitive to describing the relative ratio of D and E and furthermore did not provide a unique set of SH parameters. The same situation was encountered in analyzing the VTVH MCD data, and we found that even single-crystal HF-EPR measurements can yield D, E/D, and g values that are covariant and do not allow unique determination of their values by one set of SH parameters. Uncertainty in the SH parameters prevented a magneto-structural correlation in these $[Co(SR)_4]^{2-}$ complexes, despite the elapse of over two decades since the first reported magnetic analyses of these species. To overcome this challenge, we applied FD-FT THz-EPR measurements to directly elucidate $|D| = 55(1)$ cm^{-1}. These parameters then permitted a re-examination of magnetometry, VTVH MCD, and HF-EPR data to accurately determine g. Similar analyses were performed on $(NEt_4)_2[Co(SPh)_4]$ (**2**), and calculated CASSCF/NEVPT2 SH values are in agreement with all experimental observations for both **1** and **2**. The overarching agreement among all of these methods permits us to confidently report the SH parameters for **1** and **2**. Further, owing to the strong agreement, we verify that the differences observed in the two complexes are directly related to slight changes of the S−Co−S angle and C−S−Co−S torsion angles around the CoS_4 core. In a wider perspective, the results provided herein highlight that concerted experimental and computational multimethod protocols are a crucial tool in the field of single-molecule magnetism. The techniques are especially critical, as is demonstrated by $[Co(SPh)_4]^{2-}$, when systems possess a large zero-field splitting. Ongoing directions in our laboratories include establishing further multimethod protocols, which will help in the design of magneto-structural correlations in other systems, with the specific aim of generating larger ZFS.

■ ASSOCIATED CONTENT

ⓢ Supporting Information

The Supporting Information is available free of charge on the ACS Publications website at DOI: 10.1021/acs.inorgchem.7b00097.

> Synthetic details, crystallographic data, and characterization data (PDF)
> Crystallographic data (CIF)
> Crystallographic data (CIF)

■ AUTHOR INFORMATION

Corresponding Authors

*E-mail for S.H.: shill@magnet.fsu.edu.
*E-mail for A.S.: alexander.schnegg@helmholtz-berlin.de.
*E-mail for E.B.: bill@mpi-muelheim.mpg.de.
*E-mail for J.R.L.: jrlong@berkeley.edu.
*E-mail for F.N.: Frank.Neese@cec.mpg.de.

ORCID

Elizaveta A. Suturina: 0000-0003-4407-1882
Thomas Weyhermüller: 0000-0002-0399-7999

Notes

The authors declare no competing financial interest.

■ REFERENCES

(1) Craig, G. A.; Murrie, M. 3d single-ion magnets. *Chem. Soc. Rev.* **2015**, *44* (8), 2135−2147.

(2) Atanasov, M.; Aravena, D.; Suturina, E.; Bill, E.; Maganas, D.; Neese, F. First principles approach to the electronic structure, magnetic anisotropy and spin relaxation in mononuclear 3d-transition metal single molecule magnets. *Coord. Chem. Rev.* **2015**, *289−290*, 177−214.

(3) Graeme, H.; Lawrence, B. *Metals in Biology: Applications of High-Resolution EPR to Metalloenzymes*; Springer: New York, 2010.

(4) Swenson, D.; Baenziger, N. C.; Coucouvanis, D. Tetrahedral mercaptide complexes. Crystal and molecular structures of [(C6H5)-4P]2M(SC6H5)4 complexes (M = cadmium(II), zinc(II), nickel(II), cobalt(II), and manganese(II)). *J. Am. Chem. Soc.* **1978**, *100* (6), 1932−1934.

(5) Coucouvanis, D. Fe-M-S complexes derived from MS42- anions (M = molybdenum, tungsten) and their possible relevance as analogs for structural features in the molybdenum site of nitrogenase. *Acc. Chem. Res.* **1981**, *14* (7), 201−209.

(6) Fukui, K.; Ohyanishiguchi, H.; Hirota, N. Esr and Magnetic-Susceptibility Studies on High-Spin Tetrahedral Cobalt(Ii)-Thiolate Complexes - an Approach to Rubredoxin-Type Active-Sites. *Bull. Chem. Soc. Jpn.* **1991**, *64* (4), 1205−1212.

(7) Makinen, M. W.; Kuo, L. C.; Yim, M. B.; Wells, G. B.; Fukuyama, J. M.; Kim, J. E. Ground term splitting of high-spin cobalt(2+) ion as a probe of coordination structure. 1. Dependence of the splitting on coordination geometry. *J. Am. Chem. Soc.* **1985**, *107* (18), 5245−5255.

(8) Bennett, B. In *Metals in Biology*; Hanson, G., Berliner, L., Eds.; Springer: New York, 2010; Chapter 10, Vol. 29, pp 345−370.

(9) Larrabee, J. A.; Alessi, C. M.; Asiedu, E. T.; Cook, J. O.; Hoerning, K. R.; Klingler, L. J.; Okin, G. S.; Santee, S. G.; Volkert, T. L. Magnetic Circular Dichroism Spectroscopy as a Probe of Geometric and Electronic Structure of Cobalt(II)-Substituted Proteins: Ground-State Zero-Field Splitting as a Coordination Number Indicator. *J. Am. Chem. Soc.* **1997**, *119* (18), 4182−4196.

(10) Banci, L.; Bencini, A.; Benelli, C.; Gatteschi, D.; Zanchini, C. In *Structures versus Special Properties*; Springer: Berlin, Heidelberg, 1982; Chapter 2, Vol. 52, pp 37−86.

(11) Fukui, K.; Masuda, H.; Ohyanishiguchi, H.; Kamada, H. Effects of Co-S Torsion Angle Variation in a Cobalt(Ii)-Thiolate Complex - X-Ray Crystal-Structure Analysis, Single-Crystal Epr Measurements and Ligand-Field Calculations. *Inorg. Chim. Acta* **1995**, *238* (1−2), 73−81.

(12) Suturina, E. A.; Maganas, D.; Bill, E.; Atanasov, M.; Neese, F. Magneto-Structural Correlations in a Series of Pseudotetrahedral [CoII(XR)4]2− Single Molecule Magnets: An ab Initio Ligand Field Study. *Inorg. Chem.* **2015**, *54*, 9948.

(13) Maganas, D.; Sottini, S.; Kyritsis, P.; Groenen, E. J. J.; Neese, F. Theoretical Analysis of the Spin Hamiltonian Parameters in Co(II)S4 Complexes, Using Density Functional Theory and Correlated ab initio Methods. *Inorg. Chem.* **2011**, *50* (18), 8741−8754.

(14) Idešicová, M.; Titiš, J.; Krzystek, J.; Boča, R. Zero-Field Splitting in Pseudotetrahedral Co(II) Complexes: a Magnetic, High-Frequency and -Field EPR, and Computational Study. *Inorg. Chem.* **2013**, *52* (16), 9409−9417.

(15) Murrie, M. Cobalt(ii) single-molecule magnets. *Chem. Soc. Rev.* **2010**, *39* (6), 1986−1995.

(16) Zadrozny, J. M.; Telser, J.; Long, J. R. Slow magnetic relaxation in the tetrahedral cobalt(II) complexes [Co(EPh)4]2− (EO, S, Se). *Polyhedron* **2013**, *64*, 209−217.

(17) Zadrozny, J. M.; Long, J. R. Slow Magnetic Relaxation at Zero Field in the Tetrahedral Complex [Co(SPh)4]2−. *J. Am. Chem. Soc.* **2011**, *133* (51), 20732−20734.

(18) Zadrozny, J. M.; Liu, J.; Piro, N. A.; Chang, C. J.; Hill, S.; Long, J. R. Slow magnetic relaxation in a pseudotetrahedral cobalt(ii) complex with easy-plane anisotropy. *Chem. Commun.* **2012**, *48* (33), 3927−3929.

(19) Vaidya, S.; Tewary, S.; Singh, S. K.; Langley, S. K.; Murray, K. S.; Lan, Y.; Wernsdorfer, W.; Rajaraman, G.; Shanmugam, M. What Controls the Sign and Magnitude of Magnetic Anisotropy in Tetrahedral Cobalt(II) Single-Ion Magnets? *Inorg. Chem.* **2016**, *55* (19), 9564−9578.

(20) Saber, M. R.; Dunbar, K. R. Ligands effects on the magnetic anisotropy of tetrahedral cobalt complexes. *Chem. Commun.* **2014**, *50* (82), 12266−12269.

(21) Forshaw, A. P.; Smith, J. M.; Ozarowski, A.; Krzystek, J.; Smirnov, D.; Zvyagin, S. A.; Harris, T. D.; Karunadasa, H. I.; Zadrozny, J. M.; Schnegg, A.; Holldack, K.; Jackson, T. A.; Alamiri, A.; Barnes, D. M.; Telser, J. Low-Spin Hexacoordinate Mn(III): Synthesis and Spectroscopic Investigation of Homoleptic Tris(pyrazolyl)borate and Tris(carbene)borate Complexes. *Inorg. Chem.* **2013**, *52* (1), 144−159.

(22) Fataftah, M. S.; Coste, S. C.; Vlaisavljevich, B.; Zadrozny, J. M.; Freedman, D. E. Transformation of the coordination complex [Co(C3S5)2]2- from a molecular magnet to a potential qubit. *Chem. Sci.* **2016**, *7* (9), 6160−6166.

(23) Fataftah, M. S.; Zadrozny, J. M.; Rogers, D. M.; Freedman, D. E. A Mononuclear Transition Metal Single-Molecule Magnet in a Nuclear Spin-Free Ligand Environment. *Inorg. Chem.* **2014**, *53* (19), 10716−10721.

(24) Carl, E.; Demeshko, S.; Meyer, F.; Stalke, D. Triimidosulfonates as Acute Bite-Angle Chelates: Slow Relaxation of the Magnetization in Zero Field and Hysteresis Loop of a CoII Complex. *Chem. - Eur. J.* **2015**, *21* (28), 10109−10115.

(25) Ziegenbalg, S.; Hornig, D.; Görls, H.; Plass, W. Cobalt(II)-Based Single-Ion Magnets with Distorted Pseudotetrahedral [N2O2] Coordination: Experimental and Theoretical Investigations. *Inorg. Chem.* **2016**, *55* (8), 4047−4058.

(26) Rechkemmer, Y.; Breitgoff, F. D.; van der Meer, M.; Atanasov, M.; Hakl, M.; Orlita, M.; Neugebauer, P.; Neese, F.; Sarkar, B.; van Slageren, J. A four-coordinate cobalt(II) single-ion magnet with coercivity and a very high energy barrier. *Nat. Commun.* **2016**, *7*, 10467.

(27) Smolko, L.; Černák, J.; Dušek, M.; Titiš, J.; Boča, R. Tetracoordinate Co(ii) complexes containing bathocuproine and single molecule magnetism. *New J. Chem.* **2016**, *40* (8), 6593−6598.

(28) Bruno, R.; Vallejo, J.; Marino, N.; De Munno, G.; Krzystek, J.; Cano, J.; Pardo, E.; Armentano, D. Cytosine Nucleobase Ligand: A Suitable Choice for Modulating Magnetic Anisotropy in Tetrahedrally Coordinated Mononuclear CoII Compounds. *Inorg. Chem.* **2017**, DOI: 10.1021/acs.inorgchem.6b02448.

(29) Zhu, Y.-Y.; Liu, F.; Liu, J.-J.; Meng, Y.-S.; Jiang, S.-D.; Barra, A.-L.; Wernsdorfer, W.; Gao, S. Slow Magnetic Relaxation in Weak Easy-Plane Anisotropy: the Case of a Combined Magnetic and HFEPR Study. *Inorg. Chem.* **2017**, *56* (2), 697−700.

(30) Krzystek, J.; Telser, J. Measuring giant anisotropy in paramagnetic transition metal complexes with relevance to single-ion magnetism. *Dalton Trans.* **2016**, *45* (42), 16751−16763.

(31) Pilbrow, J. R. Effective g values for S = 3/2 and S = 5/2. *J. Magn. Reson.* **1978**, *31* (3), 479−490.

(32) Telser, J.; Krzystek, J.; Ozarowski, A. High-frequency and high-field electron paramagnetic resonance (HFEPR): a new spectroscopic tool for bioinorganic chemistry. *JBIC, J. Biol. Inorg. Chem.* **2014**, *19* (3), 297−318.

(33) Krzystek, J.; Ozarowski, A.; Telser, J. Multi-frequency, high-field EPR as a powerful tool to accurately determine zero-field splitting in high-spin transition metal coordination complexes. *Coord. Chem. Rev.* **2006**, *250* (17−18), 2308−2324.

(34) Marriott, K. E. R.; Bhaskaran, L.; Wilson, C.; Medarde, M.; Ochsenbein, S. T.; Hill, S.; Murrie, M. Pushing the limits of magnetic anisotropy in trigonal bipyramidal Ni(ii). *Chem. Sci.* **2015**, *6* (12), 6823−6828.

(35) Ruamps, R.; Maurice, R.; Batchelor, L.; Boggio-Pasqua, M.; Guillot, R.; Barra, A. L.; Liu, J.; Bendeif, E.-J.; Pillet, S.; Hill, S.; Mallah, T.; Guihéry, N. Giant Ising-Type Magnetic Anisotropy in Trigonal Bipyramidal Ni(II) Complexes: Experiment and Theory. *J. Am. Chem. Soc.* **2013**, *135* (8), 3017−3026.

(36) Maganas, D.; Milikisyants, S.; Rijnbeek, J. M. A.; Sottini, S.; Levesanos, N.; Kyritsis, P.; Groenen, E. J. J. A Multifrequency High-Field Electron Paramagnetic Resonance Study of CoIIS4 Coordination. *Inorg. Chem.* **2010**, *49* (2), 595−605.

(37) Zadrozny, J. M.; Liu, J. J.; Piro, N. A.; Chang, C. J.; Hill, S.; Long, J. R. Slow magnetic relaxation in a pseudotetrahedral cobalt(II) complex with easy-plane anisotropy. *Chem. Commun.* **2012**, *48* (33), 3927−3929.

(38) Lawrence, J.; Beedle, C. C.; Yang, E. C.; Ma, J.; Hill, S.; Hendrickson, D. N. High frequency electron paramagnetic resonance (HFEPR) study of a high spin Co(II) complex. *Polyhedron* **2007**, *26* (9−11), 2299−2303.

(39) Sottini, S.; Poneti, G.; Ciattini, S.; Levesanos, N.; Ferentinos, E.; Krzystek, J.; Sorace, L.; Kyritsis, P. Magnetic Anisotropy of Tetrahedral CoII Single-Ion Magnets: Solid-State Effects. *Inorg. Chem.* **2016**, *55*, 9537.

(40) Pinkowicz, D.; Southerland, H. I.; Avendano, C.; Prosvirin, A.; Sanders, C.; Wernsdorfer, W.; Pedersen, K. S.; Dreiser, J.; Clérac, R.; Nehrkorn, J.; Simeoni, G. G.; Schnegg, A.; Holldack, K.; Dunbar, K. R. Cyanide Single-Molecule Magnets Exhibiting Solvent Dependent Reversible "On" and "Off" Exchange Bias Behavior. *J. Am. Chem. Soc.* **2015**, *137* (45), 14406−14422.

(41) Nehrkorn, J.; Schnegg, A.; Holldack, K.; Stoll, S. General Magnetic Transition Dipole Moments for Electron Paramagnetic Resonance. *Phys. Rev. Lett.* **2015**, *114* (1), 010801.

(42) Schnegg, A.; Behrends, J.; Lips, K.; Bittl, R.; Holldack, K. Frequency domain Fourier transform THz-EPR on single molecule magnets using coherent synchrotron radiation. *Phys. Chem. Chem. Phys.* **2009**, *11* (31), 6820−6825.

(43) Telser, J.; van Slageren, J.; Vongtragool, S.; Dressel, M.; Reiff, W. M.; Zvyagin, S. A.; Ozarowski, A.; Krzystek, J. High-frequency/high-field EPR spectroscopy of the high-spin ferrous ion in hexaaqua complexes. *Magn. Reson. Chem.* **2005**, *43*, S130−S139.

(44) Pedersen, K. S.; Dreiser, J.; Nehrkorn, J.; Gysler, M.; Schau-Magnussen, M.; Schnegg, A.; Holldack, K.; Bittl, R.; Piligkos, S.; Weihe, H.; Tregenna-Piggott, P.; Waldmann, O.; Bendix, J. A linear single-molecule magnet based on [Ru-III(CN)(6)](3-). *Chem. Commun.* **2011**, *47* (24), 6918−6920.

(45) Jiang, S.-D.; Maganas, D.; Levesanos, N.; Ferentinos, E.; Haas, S.; Thirunavukkuarasu, K.; Krzystek, J.; Dressel, M.; Bogani, L.; Neese, F.; Kyritsis, P. Direct Observation of Very Large Zero-Field Splitting in a Tetrahedral NiIISe4 Coordination Complex. *J. Am. Chem. Soc.* **2015**, *137* (40), 12923−12928.

(46) Sutherland, J. C.; Holmquist, B. Magnetic Circular Dichroism of Biological Molecules. *Annu. Rev. Biophys. Bioeng.* **1980**, *9* (1), 293−326.

(47) Stephens, P. J. Magnetic Circular Dichroism. *Annu. Rev. Phys. Chem.* **1974**, *25* (1), 201−232.

(48) Dooley, D. M.; Dawson, J. H. Bioinorganic applications of magnetic circular dichroism spectroscopy: Copper, rare-earth ions, cobalt and non-heme iron systems. *Coord. Chem. Rev.* **1984**, *60*, 1−66.

(49) Solomon, E. I.; Pavel, E. G.; Loeb, K. E.; Campochiaro, C. Magnetic circular dichroism spectroscopy as a probe of the geometric and electronic structure of non-heme ferrous enzymes. *Coord. Chem. Rev.* **1995**, *144*, 369−460.

(50) Neese, F.; Solomon, E. I. MCD C-term signs, saturation behavior, and determination of band polarizations in randomly oriented systems with spin S ≥ 1/2. Applications to S = 1/2 and S = 5/2. *Inorg. Chem.* **1999**, *38* (8), 1847−1865.

(51) Oganesyan, V. S.; George, S. J.; Cheesman, M. R.; Thomson, A. J. A novel, general method of analyzing magnetic circular dichroism spectra and magnetization curves of high-spin metal ions: Application to the protein oxidized rubredoxin, Desulfovibrio gigas. *J. Chem. Phys.* **1999**, *110* (2), 762−777.

(52) Oganesyan, V. S.; Thomson, A. J. Magnetic circular dichroism of symmetry and spin forbidden transitions of high-spin metal ions. *J. Chem. Phys.* **2000**, *113* (12), 5003−5017.

(53) McInnes, E. J. L.; Pidcock, E.; Oganesyan, V. S.; Cheesman, M. R.; Powell, A. K.; Thomson, A. J. Optical Detection of Spin Polarization in Single-Molecule Magnets [Mn12O12(O2CR)16-(H2O)4]. *J. Am. Chem. Soc.* **2002**, *124* (31), 9219−9228.

(54) Cheesman, M. R.; Oganesyan, V. S.; Watmough, N. J.; Butler, C. S.; Thomson, A. J. The Nature of the Exchange Coupling between High-Spin Fe(III) Heme o3 and CuB(II) in Escherichia coli Quinol Oxidase, Cytochrome bo3: MCD and EPR Studies. *J. Am. Chem. Soc.* **2004**, *126* (13), 4157−4166.

(55) Oganesyan, V. S.; Cheesman, M. R.; Thomson, A. J. Magnetic Circular Dichroism Evidence for a Weakly Coupled Heme-Radical Pair at the Active Site of Cytochrome cd1, a Nitrite Reductase. *Inorg. Chem.* **2007**, *46* (26), 10950−10952.

(56) Gómez-Coca, S.; Aravena, D.; Morales, R.; Ruiz, E. Large magnetic anisotropy in mononuclear metal complexes. *Coord. Chem. Rev.* **2015**, *289−290*, 379−392.

(57) Durand, P.; Malrieu, J.-P. In *Advances in Chemical Physics*; Wiley: Hoboken, NJ, 2007; pp 321−412.

(58) Ye, S.; Kupper, C.; Meyer, S.; Andris, E.; Navrátil, R.; Krahe, O.; Mondal, B.; Atanasov, M.; Bill, E.; Roithová, J.; Meyer, F.; Neese, F. Magnetic Circular Dichroism Evidence for an Unusual Electronic Structure of a Tetracarbene−Oxoiron(IV) Complex. *J. Am. Chem. Soc.* **2016**, *138*, 14312.

(59) Ye, S.; Xue, G.; Krivokapic, I.; Petrenko, T.; Bill, E.; Que, L., Jr; Neese, F. Magnetic circular dichroism and computational study of mononuclear and dinuclear iron(iv) complexes. *Chem. Sci.* **2015**, *6* (5), 2909−2921.

(60) White, R. M. *Quantum theory of magnetism: magnetic properties of materials*, 3rd completely revised ed.; Springer: Berlin, New York, 2007.

(61) Takahashi, S.; Hill, S. Rotating cavity for high-field angle-dependent microwave spectroscopy of low-dimensional conductors and magnets. *Rev. Sci. Instrum.* **2005**, *76* (2), 023114.

(62) Mola, M.; Hill, S.; Goy, P.; Gross, M. Instrumentation for millimeter-wave magnetoelectrodynamic investigations of low-dimensional conductors and superconductors. *Rev. Sci. Instrum.* **2000**, *71* (1), 186−200.

(63) Holldack, K.; Schnegg, A. THz Electron Paramagnetic Resonance/THz Spectroscopy at BESSY II. *Journal of large-scale research facilities* **2016**, *2*, A51.

(64) Abo-Bakr, M.; Feikes, J.; Holldack, K.; Kuske, P.; Peatman, W. B.; Schade, U.; Wüstefeld, G.; Hübers, H. W. Brilliant, Coherent Far-Infrared (THz) Synchrotron Radiation. *Phys. Rev. Lett.* **2003**, *90* (9), 094801.

(65) Nehrkorn, J.; Telser, J.; Holldack, K.; Stoll, S.; Schnegg, A. Simulating Frequency-Domain Electron Paramagnetic Resonance: Bridging the Gap between Experiment and Magnetic Parameters for High-Spin Transition-Metal Ion Complexes. *J. Phys. Chem. B* **2015**, *119* (43), 13816−13824.

(66) Stoll, S.; Schweiger, A. EasySpin, a comprehensive software package for spectral simulation and analysis in EPR. *J. Magn. Reson.* **2006**, *178* (1), 42−55.

(67) Neese, F. The ORCA program system. *WIREs Comput. Mol. Sci.* **2012**, *2* (1), 73−78.

(68) Becke, A. D. Density-Functional Exchange-Energy Approximation with Correct Asymptotic-Behavior. *Phys. Rev. A: At., Mol., Opt. Phys.* **1988**, *38* (6), 3098−3100.

(69) Perdew, J. P. Density-Functional Approximation for the Correlation-Energy of the Inhomogeneous Electron-Gas. *Phys. Rev. B: Condens. Matter Mater. Phys.* **1986**, *33* (12), 8822−8824.

(70) Schäfer, A.; Huber, C.; Ahlrichs, R. Fully optimized contracted Gaussian basis sets of triple zeta valence quality for atoms Li to Kr. *J. Chem. Phys.* **1994**, *100* (8), 5829−5835.

(71) Weigend, F.; Ahlrichs, R. Balanced basis sets of split valence, triple zeta valence and quadruple zeta valence quality for H to Rn: Design and assessment of accuracy. *Phys. Chem. Chem. Phys.* **2005**, *7* (18), 3297−3305.

(72) Schäfer, A.; Horn, H.; Ahlrichs, R. Fully optimized contracted Gaussian basis sets for atoms Li to Kr. *J. Chem. Phys.* **1992**, *97* (4), 2571−2577.

(73) Grimme, S.; Antony, J.; Ehrlich, S.; Krieg, H. A consistent and accurate ab initio parametrization of density functional dispersion correction (DFT-D) for the 94 elements H-Pu. *J. Chem. Phys.* **2010**, *132* (15), 154104.

(74) Grimme, S.; Ehrlich, S.; Goerigk, L. Effect of the Damping Function in Dispersion Corrected Density Functional Theory. *J. Comput. Chem.* **2011**, *32* (7), 1456−1465.

(75) Neese, F. An improvement of the resolution of the identity approximation for the formation of the Coulomb matrix. *J. Comput. Chem.* **2003**, *24* (14), 1740−1747.

(76) Ganyushin, D.; Neese, F. First-principles calculations of magnetic circular dichroism spectra. *J. Chem. Phys.* **2008**, *128* (11), 114117.

(77) Roos, B. O.; Taylor, P. R.; Siegbahn, P. E. M. A Complete Active Space SCF Method (CASSCF) Using a Density-Matrix Formulated Super-CI Approach. *Chem. Phys.* **1980**, *48* (2), 157−173.

(78) Siegbahn, P. E. M.; Almlof, J.; Heiberg, A.; Roos, B. O. The Complete Active Space SCF (CASSCF) Method in a Newton-Raphson Formulation with Application to the HNO Molecule. *J. Chem. Phys.* **1981**, *74* (4), 2384−2396.

(79) Angeli, C.; Cimiraglia, R.; Evangelisti, S.; Leininger, T.; Malrieu, J.-P. Introduction of n-electron valence states for multireference perturbation theory. *J. Chem. Phys.* **2001**, *114* (23), 10252−10264.

(80) Angeli, C.; Cimiraglia, R. Multireference perturbation configuration interaction V. Third-order energy contributions in the Møller−Plesset and Epstein−Nesbet partitions. *Theor. Chem. Acc.* **2002**, *107* (5), 313−317.

(81) Pantazis, D. A.; Chen, X. Y.; Landis, C. R.; Neese, F. All-electron scalar relativistic basis sets for third-row transition metal atoms. *J. Chem. Theory Comput.* **2008**, *4* (6), 908−919.

(82) Hess, B. A. Relativistic Electronic-Structure Calculations Employing a 2-Component No-Pair Formalism with External-Field Projection Operators. *Phys. Rev. A: At., Mol., Opt. Phys.* **1986**, *33* (6), 3742−3748.

(83) Ganyushin, D.; Neese, F. A fully variational spin-orbit coupled complete active space self-consistent field approach: application to electron paramagnetic resonance g-tensors. *J. Chem. Phys.* **2013**, *138* (10), 104113.

(84) Vallet, V.; Maron, L.; Teichteil, C.; Flament, J.-P. A two-step uncontracted determinantal effective Hamiltonian-based SO−CI method. *J. Chem. Phys.* **2000**, *113* (4), 1391−1402.

(85) Maurice, R.; Bastardis, R.; Graaf, C. d.; Suaud, N.; Mallah, T.; Guihéry, N. Universal Theoretical Approach to Extract Anisotropic Spin Hamiltonians. *J. Chem. Theory Comput.* **2009**, *5* (11), 2977−2984.

(86) Zadrozny, J. M.; Atanasov, M.; Bryan, A. M.; Lin, C.-Y.; Rekken, B. D.; Power, P. P.; Neese, F.; Long, J. R. Slow magnetization dynamics in a series of two-coordinate iron(ii) complexes. *Chem. Sci.* **2013**, *4* (1), 125−138.

(87) Boudreaux, E. A.; Mulay, L. N. *Theory and applications of molecular paramagnetism*; Wiley: New York, 1976.

(88) Kahn, O. *Molecular Magnetism*; Wiley: New York, 1993.

(89) Fukui, K.; Kojima, N.; Ohyanishiguchi, H.; Hirota, N. Metal Thiolate Bonding Properties - Single-Crystal Esr, Susceptibility, and Polarized Absorption Evidence for a Strong Pi-Interaction in Tetrakis(Thiophenolato)Cobaltate(Ii). *Inorg. Chem.* **1992**, *31* (8), 1338−1344.

(90) Vrajmasu, V. V.; Munck, E.; Bominaar, E. L. Theoretical analysis of the three-dimensional structure of tetrathiolato iron complexes. *Inorg. Chem.* **2004**, *43* (16), 4867−4879.